PHYSICAL REVIEW FLUIDS **7**, 044607 (2022)

Three-dimensional direct numerical simulations of vortex-induced vibrations of a circular cylinder in proximity to a stationary wall

Weilin Chen,[1] Chunning Ji,[1,2,*] Dong Xu,[1,2] and Zhimeng Zhang[1]
[1] *State Key Laboratory of Hydraulic Engineering Simulation and Safety, Tianjin University, Tianjin 300072, China*
[2] *Key Laboratory of Earthquake Engineering Simulation and Seismic Resilience of China Earthquake Administration, Tianjin University, Tianjin 300350, China*

(Received 17 January 2021; accepted 14 April 2022; published 28 April 2022)

In this paper, we present three-dimensional direct numerical simulations (3D DNS) of vortex-induced vibrations of an elastically mounted circular cylinder near a stationary wall at a subcritical Reynolds number of 500. The circular cylinder can oscillate in both the streamwise and transverse directions. A typical gap of $0.8D$ between the cylinder surface and the stationary wall was selected to evaluate the characteristics of the responses and vortex dynamics in the presence of a stationary wall and boundary layer. We observe that the vibration response is two-branched, with two desynchronization regions lying at the ends of the simulated U_r range. Because of the wall proximity, the dominant vibration frequencies in the two directions are generally identical, and the trajectories of the displacement significantly differ in each branch. Figure-eight, combined figure-eight and raindrop, raindrop, and chaotic trajectories appear successively with increasing U_r, dominating the first desynchronization region, initial branch, lower branch (LB), and second desynchronization region (DS-II), respectively. In addition, the phase lag between the lift and displacement jumps from 0° to 180° at the transition between the LB and DS-II. Furthermore, we evaluated the three-dimensionality of the wake through the instantaneous vortical structures, spanwise-averaged vorticity contours, and statistics of the enstrophies. We found that the three-dimensionality increases linearly with the amplitude, leading to substantial variations in the vortex dynamics. The statistics of the gap flow indicates that the mean gap flow velocity is determined by only the time-averaged gap, whereas the fluctuating gap flow velocity is governed by the amplitude. Finally, the flow physics behind the response was analyzed using the time histories of the displacement, gap flow velocity, drag and lift coefficients, and vorticity contours in one vibration period. We observed that the interactions of the vortices with the wall-generated boundary layer play significant roles in altering the cylinder vibration. In the small-amplitude case, the boundary layer merges with the freestream-side vortex of the cylinder, forcing the gap-side vortex to pair with the freestream-side vortex. In contrast, in the large-amplitude case, the gap-side shear layer collides with the boundary layer and disintegrates into small parts, resulting in negative vortices in the wake.

DOI: 10.1103/PhysRevFluids.7.044607

I. INTRODUCTION

The vortex-induced vibration (VIV) of a circular cylinder in unbounded flow has been extensively investigated in the past several decades due to its scientific and practical significance. The theory behind this fluid-structure interaction (FSI) issue has been established. Relevant studies have been

---

[*] cnji@tju.edu.cn

reported in several review papers and books [1–7]. However, engineering applications, such as marine pipelines above the seabed, heat exchanger tubes adjacent to walls in a nuclear reactor, and chimneys near tall buildings, are frequently encountered. Compared to the wall-free configuration, the wall confinement and boundary layer can drastically alter the vibration and vortex dynamics of cylindrical structures. In this study, we focus on the three-dimensional flow characteristics and vibration behaviors of a circular cylinder near a stationary wall in the subcritical flow regime, and we explore the flow physics of near-wall VIV.

Both the vibration and vortex dynamics of a circular cylinder close to a stationary wall are significantly altered by the wall confinement and interactions with the boundary layer. Tsahalis and Jones [8] found that unlike the figure-eight trajectories of an unbounded cylinder, the trajectories of a cylinder near a flat plane are oval-shaped. Similar results were reported by Kozakiewicz *et al.* [9]. Chern *et al.* [10] numerically observed that the presence of a boundary layer can lead to increased streamwise amplitude and decreased transverse amplitude. Fredsøe *et al.* [11] showed that when the reduced velocity $U_r = U_\infty / f_n D$ (U_∞ is the incoming flow velocity, f_n is the natural frequency of the cylinder, and D is the cylinder diameter) is less than 3 and the gap ratio G/D (G is the distance between the cylinder surface and the stationary wall) is larger than 0.3, the transverse vibration frequency is close to the vortex shedding frequency of a stationary cylinder but deviates when $3 < U_r < 8$ and $G/D < 1$. Raghavan *et al.* [12] found that at $G/D < 3.0$, the wall-generated boundary layer has a strong impact on the vibration response, vortex shedding frequency, and onset of lock-in. Moreover, they observed that the vibration amplitude also depends strongly on the Reynolds number Re ($=U_\infty D/\nu$, where ν is the kinematic viscosity) and the normalized boundary layer thickness δ/D (δ is the boundary layer thickness). Yang *et al.* [13] experimentally discovered that with increasing G/D, the vibration amplitude increases, but the vibration frequency varies slightly when $G/D > 0.66$. In addition, the cylinder vibration is easier to initiate in the presence of the plane boundary. Fu *et al.* [14] experimentally observed that wall effects can accelerate vortex shedding and force the occurrence of lock-in at a higher frequency. Li *et al.* [15] numerically found that in near-wall VIV, the streamwise amplitude is significantly amplified. Similar results were reported by Chen *et al.* [16,17]. Tham *et al.* [18] found that with decreasing G/D, the lock-in width increases, and a third branch, between the initial branch (IB) and the lower branch (LB), appears at $G/D \leqslant 0.6$. Barbosa *et al.* [19] observed that at a large G/D (>2.0), the vibration amplitude of the lock-in region is not affected by the wall proximity. At an intermediate G/D ($=0.75$–2.0), the vibration amplitude decreases while the oscillation remains symmetric to the equilibrium position. At a small G/D (<0.75), asymmetric vibration appears, and the cylinder may collide with the stationary wall in some cases. Zhao and Cheng [20] numerically observed that VIV can be excited even when G/D is 0.002, at which the vortex shedding of the inner shear layer is completely suppressed in the stationary case. Chung [21] numerically studied the transverse VIV of a circular cylinder near a stationary wall at $G/D = 0.06$, 0.3, and 31.5, and found that with increasing G/D, the lock-in width increases while the maximum vibration amplitude decreases. In addition, the time-averaged lift is positive for all three G/D cases, suggesting repulsive cylinder-wall interactions.

Regarding the vortex-shedding patterns, Wang *et al.* [22] conducted a series of water channel experiments on the near-wall VIV of a circular cylinder at $G/D = 0.05$–2.5 and $U_r = 1.53$–6.62 with a mass ratio m^* ($=m/m_f$, where m is the cylinder mass and m_f is the displaced fluid mass) of 1.0. They found that at small values of G/D, the vortices are only shed from the freestream side, leading to a single-side vortex shedding pattern. However, at large G/D, two rows of vortices occur due to the weak wall effects. Li *et al.* [23] identified four vortex-shedding patterns from the near-wall VIV, referred to as W2S(A) (comparable vortices shed from both sides of the cylinder), W2S(B) [similar to W2S(A) but with weaker gap-side vortices], 1S (no vortex shed from the gap side), and NS (no vortex shed from both sides). Daneshvar and Morton [24] experimentally found that the cylinder amplitude increases as G/D decreases. When G/D is smaller than a critical value, a collision between the cylinder and the stationary wall occurs. Six different types of vortex-shedding patterns were found, namely 2S, 2P, 2S+S, 2P+S, S, and P. The latter two arise when significant suppression of the gap-side shear layer occurs. In the 2S pattern, one vortex is shed from each side of the cylinder in one vibration period, while in the 2P pattern, two vortices are shed from each side of the cylinder [25]. The 2S+S and 2P+S patterns are similar to the 2S and 2P patterns with an extra vortex separated from the uplifted boundary layer. When the vortex shedding at the gap side is suppressed, one or two vortices are shed from the freestream side of the cylinder, leading to the occurrence of the S or P pattern. Gao *et al.* [26] numerically studied surface roughness effects on near-wall VIV and found three vortex-shedding patterns, i.e., 2S, P+S, and 2P, with the former dominating a major part of the simulated parametric range. Here, P+S indicates the wake mode with a vortex pair shed from the freestream side while a single vortex is shed from the gap side. Chen and Wu [27] numerically observed that the gap-side vortices of the cylinder are completely suppressed at $G/D < 0.5$, resulting in the 1S pattern. Peter and De [28] observed from a forced near-wall system that when the forced vibration frequency is close to the stationary vortex-shedding frequency, the vortices are shed from both sides at a larger gap distance. In contrast, when a higher frequency is applied, multiple interconnected vortices appear in the wake.

From the above literature review, it is clear that although the VIV of a circular cylinder near a plane boundary has been widely investigated, three-dimensional (3D) wake structures, providing detailed information regarding the spatiotemporal variations of the near-wall VIV, are still scarce. In this study, we focus on the vibration response and vortex dynamics of the near-wall VIV with varying U_r by performing 3D direct numerical simulations (DNSs). Both the wake three-dimensionality and the flow physics are elucidated. A subcritical Re of 500 is adopted and the gap ratio is constant at $G/D = 0.8$, at which the interaction between the vibrating cylinder and the stationary wall is violent [16,18,19]. The remainder of this paper is structured as follows. In Sec. II, the details of the adopted numerical methodology and validation cases are given. In Sec. III, the hydrodynamic forces, vibration amplitude, spectral frequencies, trajectories of the displacement, wake three-dimensionality, gap flow velocity, time-averaged flow fields, and flow physics for each region are presented. In Sec. IV, the main findings of this study are summarized.

II. NUMERICAL METHODOLOGY AND VALIDATION CASE

The governing equations for the fluid flow are the incompressible Navier-Stokes equations defined as follows:

$$\frac{\partial \mathbf{u}}{\partial t} + \nabla \cdot (\mathbf{u}\mathbf{u}) = -\nabla p + \nabla(\nu(\nabla \mathbf{u} + \nabla \mathbf{u}^t)), \tag{1}$$

$$\nabla \cdot \mathbf{u} = 0, \tag{2}$$

where $\mathbf{u}$ is the velocity, p is the pressure, ∇ denotes the gradient operator, and ν is the kinematic viscosity. The two-step predictor-corrector procedure is adopted for the decoupling of the flow governing equations, and the resultant pressure Poisson equation is solved using the BiCGSTAB (Biconjugate gradient stabilized method) [29]. The second-order Adams-Bashforth time marching scheme—a numerical method for solving ordinary differential equations, in particular the initial value problem, is employed to calculate the new velocity field.

The dynamics of an elastically supported circular cylinder is simplified as a mass-damper-spring system. In this study, the cylinders are free to oscillate in both the streamwise and transverse directions, and the governing equations of the cylinder motions are as follows:

$$m\ddot{x} + c\dot{x} + kx = F_D, \tag{3}$$

$$m\ddot{y} + c\dot{y} + ky = F_L, \tag{4}$$

where m is the mass of the cylinder, c is the structural damping, k is the stiffness coefficient, x and y are the displacement in the streamwise and transverse directions, respectively, and F_D and F_L are the drag and lift, respectively. The governing equations for cylinder motion are based on

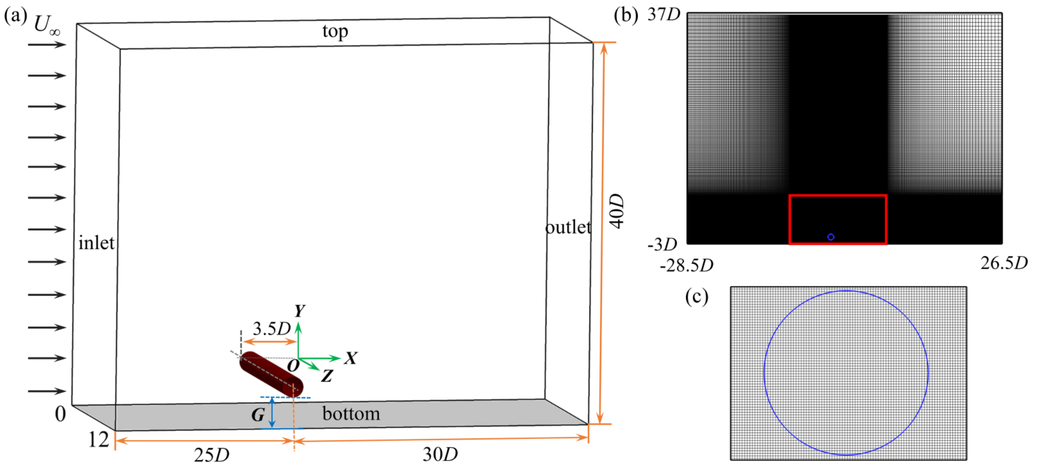

FIG. 1. (a) Computational domain and boundary conditions, (b) mesh settings in the x-y plane, and (c) mesh around the cylinder for the near-wall VIV of a circular cylinder at Re = 500. The rectangular region (red) in (b) denotes the uniform mesh region. The center of the cylinder is at $(x, y) = (-3.5D, -1.7D)$.

Newton's second law and are solved using the second-order Newmark-β method—a method of numerical integration used to solve differential equations and widely used in numerical evaluation of the dynamic response of structures.

The fluid-structure interaction (FSI) is simulated using the immersed boundary method (IBM), which was first introduced by Peskin [30] to simulate the blood flow around the flexible leaflet of a human heart. In the framework of the IB method, the flow governing equations are discretized on a fixed Cartesian grid which generally does not conform to the geometry of the moving solids. As a result, the boundary conditions on the fluid-cylinder interface, manifesting the interaction between the fluid and the structure, cannot be imposed directly. Instead, an extra body force is added to the momentum equation using interpolation and distribution functions to take such interaction into account. For the sake of conciseness, the readers are referred to our previous works [31–34] to obtain further details of the methodology.

In the present 3D DNS, the streamwise and transverse lengths of the computational domain are L_x $(=L_1 + L_2) = 55D$ and $H = 40D$, respectively [Fig. 1(a)]. Here, L_1 $(=25D)$ and L_2 $(=30D)$ denote the lengths of the no-slip wall upstream and downstream of the cylinder center, respectively. To guarantee the accuracy of the numerical results, a rectangular region of $9D \times 6D$ is discretized using a uniform mesh with a nondimensional grid spacing of $\Delta x/D$ $(\Delta y/D) = 1/64$ in both the streamwise and transverse directions. Outside this region, a stretched mesh is adopted to maintain the total grid number within an affordable range. In the spanwise direction, the cylinder length is $12D$ with a resolution of $\Delta z = 0.0625D$. A Dirichlet-type boundary ($u = U_\infty$, $v = 0$, $w = 0$) is adopted at the inflow, whereas a Neumann-type boundary ($\partial u/\partial x = 0$, $\partial v/\partial x = 0$, $\partial w/\partial x = 0$) is employed at the outflow; further, the top boundary is free-slip ($\partial u/\partial y = 0$, $v = 0$, $\partial w/\partial y = 0$), while the bottom boundary is no-slip ($u = v = w = 0$). The periodic boundary condition is applied in the z direction. The no-slip boundary condition is applied on the cylinder surface, that is, the fluid velocity is the same as the vibration velocity of the cylinder.

In the simulations of VIV of a circular cylinder in proximity to a stationary wall, the Reynolds number based on the incoming flow velocity is Re = 500 and the mass ratio of the cylinder is $m^* = 2.0$. Given the fact that when $G/D > 1.0$ the proximity wall effects become insignificant [15,19,22,35], $G/D = 0.8$ is adopted for exploring the changes in the response and vortex dynamics caused by the stationary wall. The reduced velocity is $U_r = U_\infty/f_nD = 1.0$–$9.0$, where f_n $(=\frac{1}{2\pi}\sqrt{k/m})$ is the natural frequency of the cylinder. Note that, in this study, U_r is varied by

TABLE I. Comparison of the amplitude, hydrodynamic forces, and vibration frequency for the VIV of an isolated circular cylinder at Re = 500, $U_r = 6.0$, and $m^* = 2.0$. The cylinder vibrates in both the transverse and streamwise directions.

	A_x	A_y	$\bar{C}_D$	St
Wang *et al.* [36]	0.028	0.634	1.647	0.167
Present	0.0277	0.621	1.571	0.162
Difference (%)	1.1	2.1	4.6	3.0

changing the spring stiffness (k). The structural damping ratio is set as zero to achieve larger vibrations. According to the distance ($L_1 = 25D$) of the inlet boundary to the cylinder center, the normalized boundary layer thickness is $\delta/D = 1.12$ at the cylinder center if the cylinder is absent. In this study, the circular cylinder can oscillate in both the streamwise and transverse directions.

The nondimensional amplitudes in two directions are defined as $A_x = \sqrt{2}x_{\text{rms}}/D$ and $A_y = \sqrt{2}y_{\text{rms}}/D$, respectively, where x_{rms} and y_{rms} are the rms values of the displacement in the streamwise and transverse directions. The spanwise-averaged drag (C_D) and lift (C_L) coefficients are $C_D = F_D/\frac{1}{2}\rho U_\infty^2 DL_z$ and $C_L = F_L/\frac{1}{2}\rho U_\infty^2 DL_z$, respectively, where F_D and F_L are the drag and lift forces on the cylinder, and L_z is the cylinder length. $\bar{C}_D$, $\bar{C}_L$, C_D', and C_L' are the mean drag and lift coefficients and the rms drag and lift coefficients, respectively. The phase lag (φ) between the lift and the transverse displacement is obtained through the Hilbert transform (HT). The spectra of the displacement and hydrodynamic forces are obtained through the fast Fourier transform (FFT).

The numerical method is validated through the VIV of an isolated circular cylinder at Re = 500. According to the comparative study, the circular cylinder is vibrated in both the transverse and streamwise directions. The computational domain sizes are the same as those ($X \times Y \times Z = 40D \times 20D \times 12D$) in Wang *et al.* [36]. As indicated in Table I, the results agree well with the published data, suggesting a high accuracy of the present simulations.

Further, to ensure that the adopted L_2 and H is large enough, simulations with a doubled L_2 or a doubled H were performed for the VIV of a circular cylinder in proximity to a stationary wall at $U_r = 5.0$. It is seen from Table II that the results of $L_2 = 30D$ and $H = 40D$ agree well with those of the doubled-L_2 and doubled-H cases, indicating that the adopted L_2 and H are appropriate for the simulations. Moreover, the grid convergence study for flow past a circular cylinder at Re = 500 in our previous work [37] proves that the results at $\Delta x/D$ ($\Delta y/D$) = 1/64 are well within the asymptotic range of the convergence. For the sake of conciseness, the details are not given here, and readers are referred to Chen *et al.* [37].

III. RESULTS AND DISCUSSION

A. Time histories of the displacements, vibration amplitudes, and frequencies

Figure 2 shows the time histories of the displacements in the streamwise and transverse directions at different reduced velocities. In general, at most reduced velocities, the streamwise displacement

TABLE II. Comparison of the results for VIV of a circular cylinder in proximity to a stationary wall at $L_2 = 30D$, $H = 40D$, with those at a doubled L_2 or a doubled H. Other parameters are Re = 500, $G/D = 0.8$, $U_r = 5.0$, and $m^* = 2.0$. The cylinder vibrates in both the transverse and streamwise directions.

	$\bar{C}_D$	C_D'	$\bar{C}_L$	A_x	A_y	St
$L_2 = 30D$, $H = 40D$	1.561	0.153	0.076	0.091	0.407	0.189
$L_2 = 60D$, $H = 40D$	1.579	0.155	0.076	0.092	0.408	0.187
$L_2 = 30D$, $H = 80D$	1.559	0.153	0.076	0.091	0.408	0.191

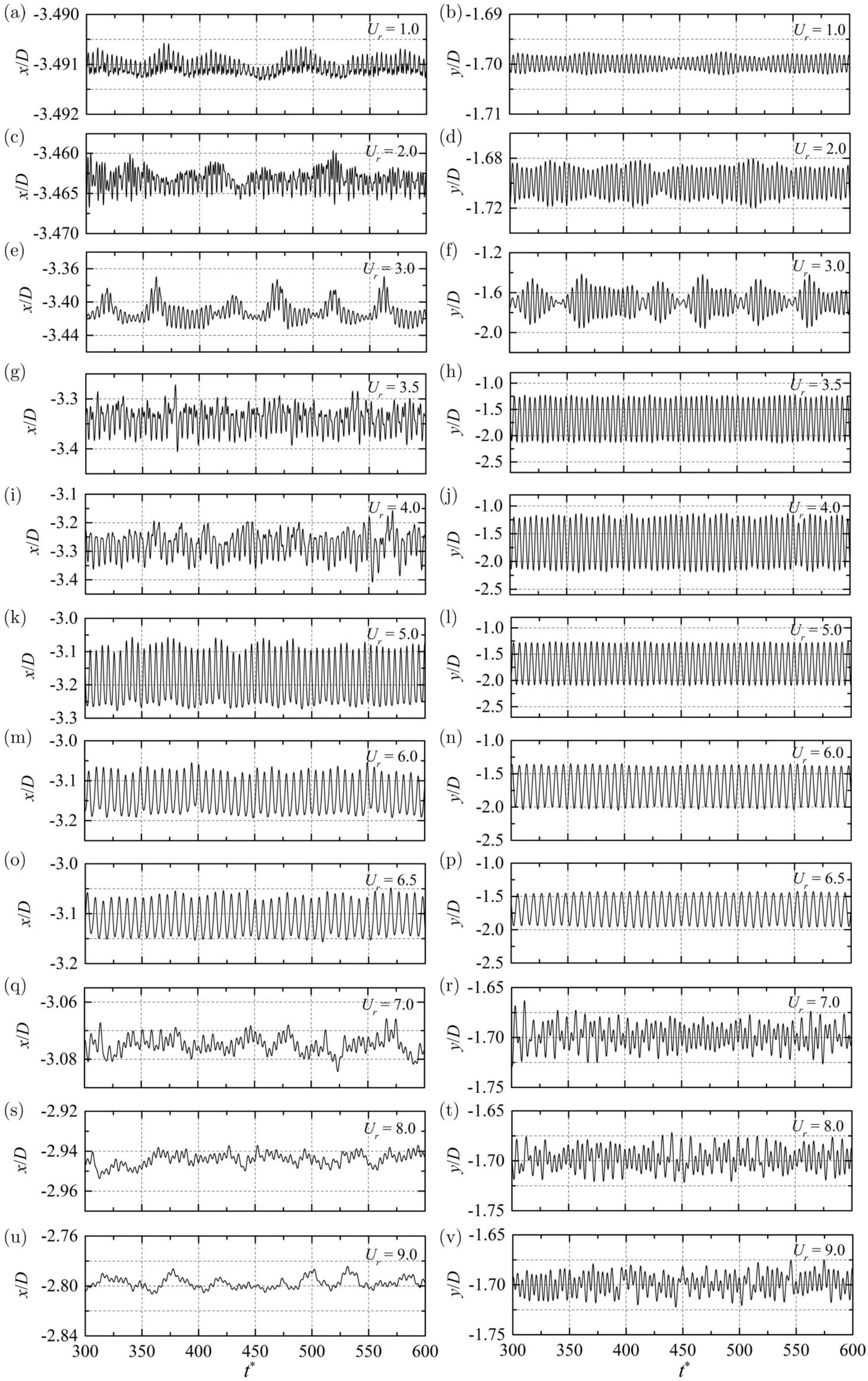

FIG. 2. Time histories of the streamwise and transverse displacements in the VIV of a circular cylinder in proximity to a stationary wall at Re $= 500$ and $G/D = 0.8$. Note that at $U_r = 6.5$, t^* ranges from 500 to 800.

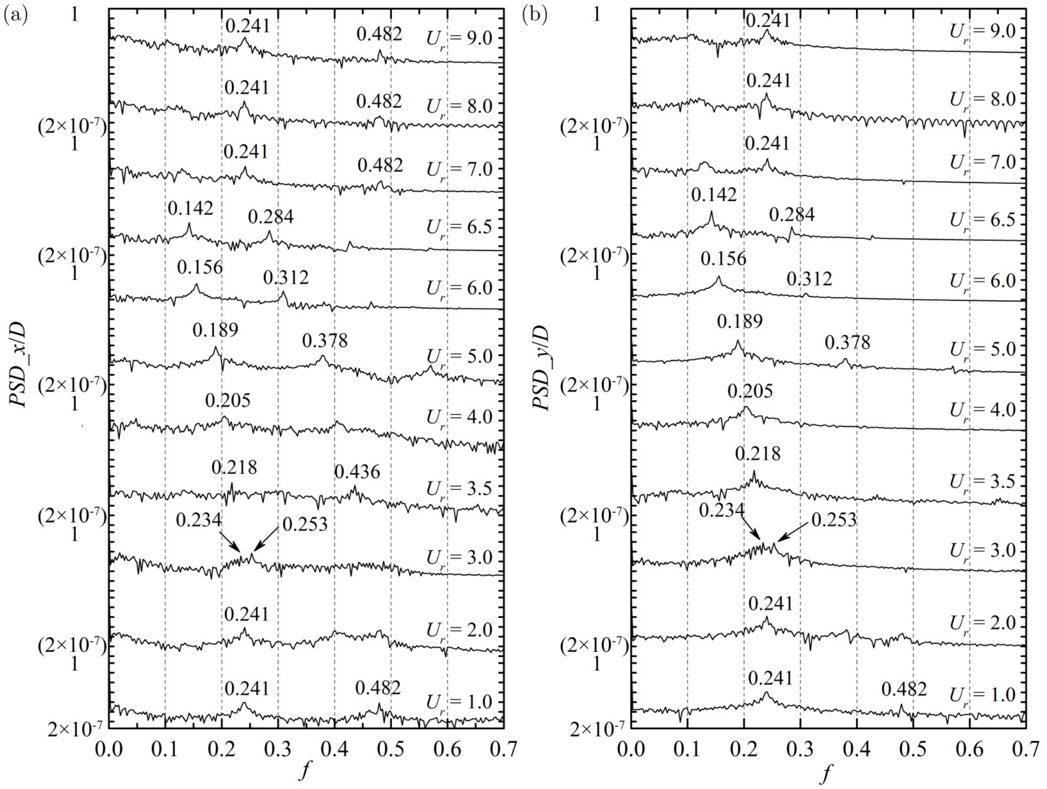

FIG. 3. Power spectral density (PSD) of the displacements in two directions for the VIV of a circular cylinder in proximity to a stationary wall at Re = 500 and $G/D = 0.8$ for (a) the streamwise displacement and (b) the transverse displacement.

is more irregular than the transverse displacement. As illustrated in Figs. 2(a) and 2(c), the streamwise displacement at $U_r = 1.0$–2.0 irregularly fluctuates with a very small range amplitude. In contrast, although the fluctuation of the transverse displacement at $U_r = 1.0$–2.0 is also small, it is approximately periodic [see Figs. 2(b) and 2(d)]. At $U_r = 3.0$, the displacements in both directions are slightly increased and resemble a synchronized beating phenomenon [Figs. 2(e) and 2(f)]. At $U_r = 3.5$, the beating behavior disappears in the displacements in both directions. The streamwise displacement remains irregular while the transverse displacement is perfectly periodic [Figs. 2(g) and 2(h)]. At $U_r = 4.0$–6.5, the displacements in both directions are significantly amplified [Figs. 2(i)–2(p)]. In this region, the transverse displacement decreases gradually with increasing U_r, a feature similar to that of a lock-in branch in an isolated circular cylinder. In addition, the transverse displacement remains periodic in this region, indicating synchronized vortex shedding along the cylinder span, while the regularity of the streamwise displacement increases slightly with increasing U_r. However, at $U_r = 7.0$–9.0, the displacements in both directions become irregular again, and the fluctuations become insignificant [Figs. 2(q)–2(v)]. Although the fluctuations at the low (=1.0–2.0) and high U_r (=7.0–9.0) are both minor, the transverse displacement in the low-U_r case is more regular than that in the high-U_r case. As will be shown later, the low-frequency components induced by the dislocations of vortex shedding along the cylinder length exhibit negligible effects on the vibration in the low-U_r case.

Figure 3 depicts the power spectral density (PSD) results of the displacements in both directions at different reduced velocities. Generally, the dominant frequencies in both directions are identical, a feature that is considerably different from that of the VIV of an isolated circular cylinder [3,38]. At

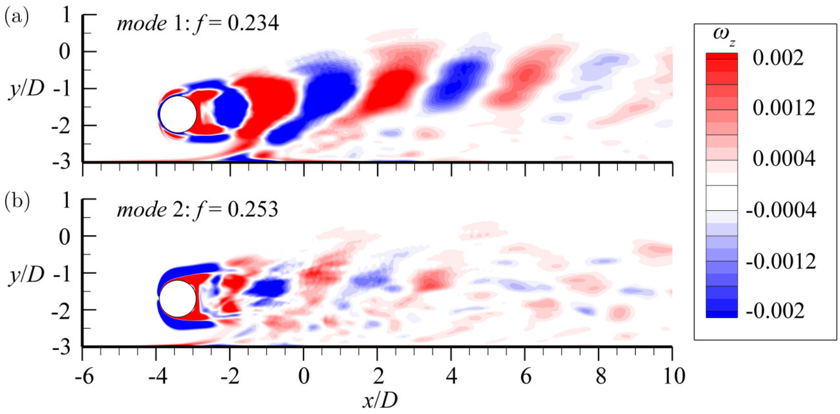

FIG. 4. The modes extracted from the z-vorticity field using DMD analysis at $U_r = 3.0$ where the beating phenomenon is observed. (a) Mode 1 at $f = 0.234$ and (b) mode 2 at $f = 0.253$.

$U_r = 1.0$–2.0, the dominant frequencies in both directions are constant at 0.241, which is the same as the vortex shedding frequency (St = 0.241) of the stationary circular cylinder. The vibration is desynchronized. At $U_r = 3.0$, corresponding to the beating phenomenon, two comparable frequencies, i.e., $f = 0.234$ and 0.253, are observed at the displacements in both directions. The beat-related frequency is 0.019, which is equal to the difference between the two comparable frequencies. The phenomenon has been reported in Navrose *et al.* [39] and Kumar *et al.* [40] that in the early stage of the initial branch (IB), the vibration frequency and the vortex shedding frequency are desynchronized, thus leading to the occurrence of the quasiperiodic behavior [40]. To identify the natures of the frequency components, the dynamic mode decomposition (DMD) of 500 snapshots of the z-vorticity ω_z at $z/D = 6.0$ was performed, with each mode consisting of a pure frequency component [41–43]. As shown in Fig. 4(a), the modal pattern at $f = 0.234$ shows the features of the Hopf bifurcation [44], corresponding to the alternate vortex-shedding of a cylinder in proximity to a plane. However, different from the symmetric DMD mode of an isolated cylinder, the DMD mode in Fig. 4(a) deflects upward because of the biased gap flow. As shown in Fig. 4(b), the modal pattern at $f = 0.253$ shows distinct features from that at $f = 0.234$, being strong around the cylinder only. The modal component dissipates quickly downstream, signifying that this mode is related to the cylinder vibration. At $U_r = 3.5$, the dominant frequencies in both directions become identical again. Although the second-harmonic frequency is observed in both directions, its component of the transverse displacement is much smaller than that of the fundamental frequency, while it becomes comparable in the streamwise displacement. At $U_r = 4.0$–6.5, the dominant frequencies in both directions are identical and decrease gradually with increasing U_r. Similar to that at $U_r = 3.5$, the second-harmonic frequency of the transverse displacement has an insignificant amplitude, and the transverse displacement is approximately periodic. However, in the streamwise displacement, the component of the second-harmonic frequency is close to that of the fundamental frequency. At $U_r = 7.0$–9.0, the dominant frequencies in both directions are constant at 0.241, which is the same as that at $U_r = 1.0$–2.0. Therefore, desynchronization dominates again. Similar to that at $U_r = 3.5$–6.5, the second-harmonic frequency is evident only in the streamwise displacement.

Figure 5 illustrates the variations in the amplitudes, vibration frequencies, and time-averaged displacements in the two directions with increasing U_r. According to the characteristics of the amplitudes and frequencies, the branches and their corresponding U_r ranges are presented in Table III. In the desynchronized branch (DS), i.e., $U_r = 1.0$–2.0 and 7.0–9.0, the amplitude is close to zero and the dominant frequency exactly follows the vortex shedding frequency (St) of the stationary case [Figs. 5(a) and 5(b)]. That is, the weak vibration does not affect the vortex shedding process. In the IB ($U_r = 3.0$–3.5), the vibration frequency deviates from the vortex shedding frequency of

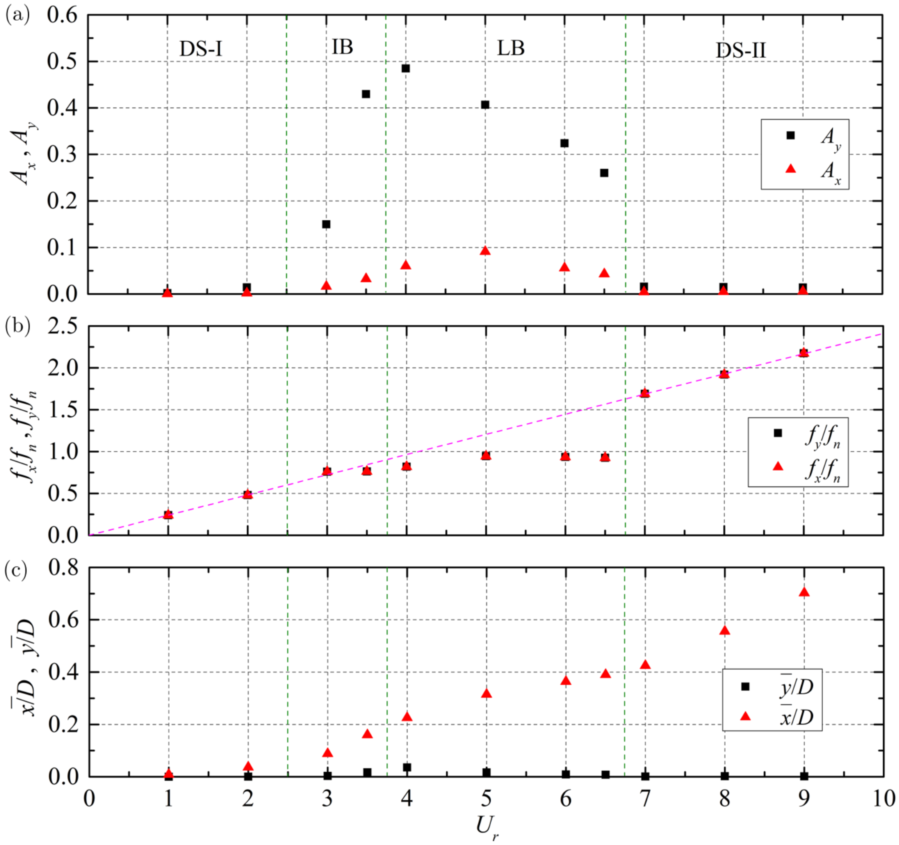

FIG. 5. Variations in the amplitudes, vibration frequencies, and shift of time-averaged displacements in the VIV of a circular cylinder in proximity to a stationary wall with U_r at Re = 500 and $G/D = 0.8$.

the stationary case, indicating the presence of soft lock-in [45,46]. In this branch, the amplitude in the transverse direction increases significantly, being much larger than the streamwise amplitude [Fig. 5(a)]. In the LB ($U_r = 4.0$–6.5), the normalized frequency (f/f_n) slightly increases from 0.81 ($U_r = 4.0$) to 0.92 ($U_r = 6.5$), signifying the occurrence of lock-in [Fig. 5(b)]. Due to the added mass effects and the low m^* (=2.0) adopted, f/f_n is slightly smaller than unity in the lock-in region. In the LB branch, the transverse displacement is approximately periodic, while the streamwise displacement is relatively irregular. The largest transverse amplitude ($A_y = 0.48$) is obtained at the beginning of this branch, while the streamwise amplitude continues to increase until $U_r = 5.0$ where the peak ($A_x = 0.09$) occurs, and afterwards it decreases slightly [Fig. 5(a)]. As will be shown later, because of the change in vortex shedding timing, there is a sudden decrease in the amplitude when transforming to the second desynchronization region (DS-II). Compared to

TABLE III. Branches and their corresponding U_r ranges for the VIV of a circular cylinder in proximity to a stationary wall at Re = 500 and $G/D = 0.8$. DS: desynchronized branch; IB: initial branch; LB: lower branch; DS-I and DS-II are the two subbranches of the DS.

Branch	DS-I	IB	LB	DS-II
U_r	1.0–2.0	3.0–3.5	4.0–6.5	7.0–9.0

the largest vibration amplitude ($A_y \sim 1.0$) in the high-Re VIV of an isolated circular cylinder, the largest vibration amplitude ($A_y = 0.48$) is substantially lower in this study, leading to the absence of the upper branch [47]. This can be attributed to the low Reynolds number ($\mathrm{Re} = 500$) adopted in this study, where the viscous effect of the fluid is relatively significant. Similar results were presented in the two-degree-of-freedom VIV of an isolated circular cylinder at the same Reynolds number in Wang *et al.* [37], with a comparable largest amplitude of $A_y = 0.634$ and showing no upper branch. The smaller largest amplitude in this study, compared to that in Wang *et al.* [37], is the fallout of the adjacent bottom wall.

Figure 5(c) shows the shift in the time-averaged displacements in both directions with increasing U_r. The shift in the transverse displacement is close to zero except at $U_r = 3.5$ and 4.0, while that in the streamwise displacement increases gradually with increasing U_r.

Figure 6 presents the trajectories and phase lags of the displacements in the two directions. Although the displacements are slightly irregular, the trajectories in the DS-I are figure-eight shaped [Figs. 6(a) and 6(b)]. In the IB, the trajectories show a combination of figure-eight and raindrop shapes, which are consistent with the presence of multiple frequencies in the streamwise displacement [Figs. 6(c) and 6(d)]. In the LB, the trajectories are raindrop-shaped, with their heads towards the upstream except at $U_r = 4.0$ [Figs. 6(e)–6(h)]. As the low frequencies become evident, the trajectories in the DS-II become completely chaotic [Figs. 6(i)–6(k)].

From the above discussion, it is clear that significant differences are induced by the presence of the stationary wall, which suggests distinct flow physics related to the response.

B. Fluid forces and spectral frequencies

Figure 7 depicts the time histories of the drag and lift coefficients at different reduced velocities. In the DS-I, the drag coefficient shows a small fluctuation, while the fluctuating lift coefficient increases significantly with increasing U_r [Figs. 7(a) and 7(b)]. In contrast, the variations in the drag and lift coefficients at $U_r = 3.0$ and 3.5 in the IB are significantly different. As indicated in Figs. 7(c) and 7(d), at $U_r = 3.0$, both the drag and lift coefficients exhibit the beating features, while at $U_r = 3.5$ they are relatively regular. Because of the increased amplitude, the fluctuating lift coefficient at $U_r = 3.5$ is significantly larger than that at $U_r = 3.0$. In the LB, consistent with the periodic displacements, both the drag and lift coefficients are relatively regular [Figs. 7(e)–7(h)]. As the amplitude decreases with increasing U_r, the fluctuating drag and lift coefficients decrease gradually. In the DS-II, the amplitudes in both directions are close to zero, and correspondingly, both the drag and lift coefficients display small fluctuations [Figs. 7(i)–7(k)]. Comparing Figs. 7(a) and 7(b) and Figs. 7(i)–7(k), the fluctuating lift coefficient in the DS-II is smaller than that in the DS-I.

Figure 8 presents the statistics of the drag and lift coefficients at different reduced velocities. As shown in Fig. 8(a), both $\bar{C}_D$ and C'_D have similar behaviors, i.e., first increasing and then decreasing with increasing U_r. In the DS-I and DS-II, both $\bar{C}_D$ and C'_D are approximately equal to those of the stationary case. The largest $\bar{C}_D$ and C'_D are observed at the same U_r (=4.0), corresponding to the beginning of the LB. Similarly, both $\bar{C}_L$ and C'_L first increase and then decrease with increasing U_r [Fig. 8(b)]. However, the peaks of C'_L and $\bar{C}_L$ are not reached at the same U_r, with the largest C'_L occurring at $U_r = 3.5$, while the largest $\bar{C}_L$ occurs at $U_r = 4.0$. This phenomenon has been reported in Chung [21], Li *et al.* [15,23], and Chen *et al.* [16], and it will be explained later.

To illustrate the forcing process and the consequent response, C_L is decomposed into two components, with one ($C_{L,a} = \frac{\sqrt{2}\tilde{C}_L y}{\sqrt{\overline{y^2}}}$) being in phase with the cylinder acceleration and the other ($C_{L,v} = \frac{\sqrt{2}\tilde{C}_L \dot{y}}{\sqrt{\overline{\dot{y}^2}}}$) being in phase with the cylinder velocity, where $\tilde{C}_L$ is the fluctuation of the lift coefficient, defined as $\tilde{C}_L = C_L - \bar{C}_L$ [48,49]. As shown in Fig. 8(c), $\bar{C}_{L,v}$ related with the energy transfer between the flow and the cylinder maintains at approximately zero in the whole U_r range. This is expected given the fact that in the self-sustained vibration, without structural damping, the time-averaged net energy transfer should be zero [49]. However, $\bar{C}_{L,a}$ remains positive until

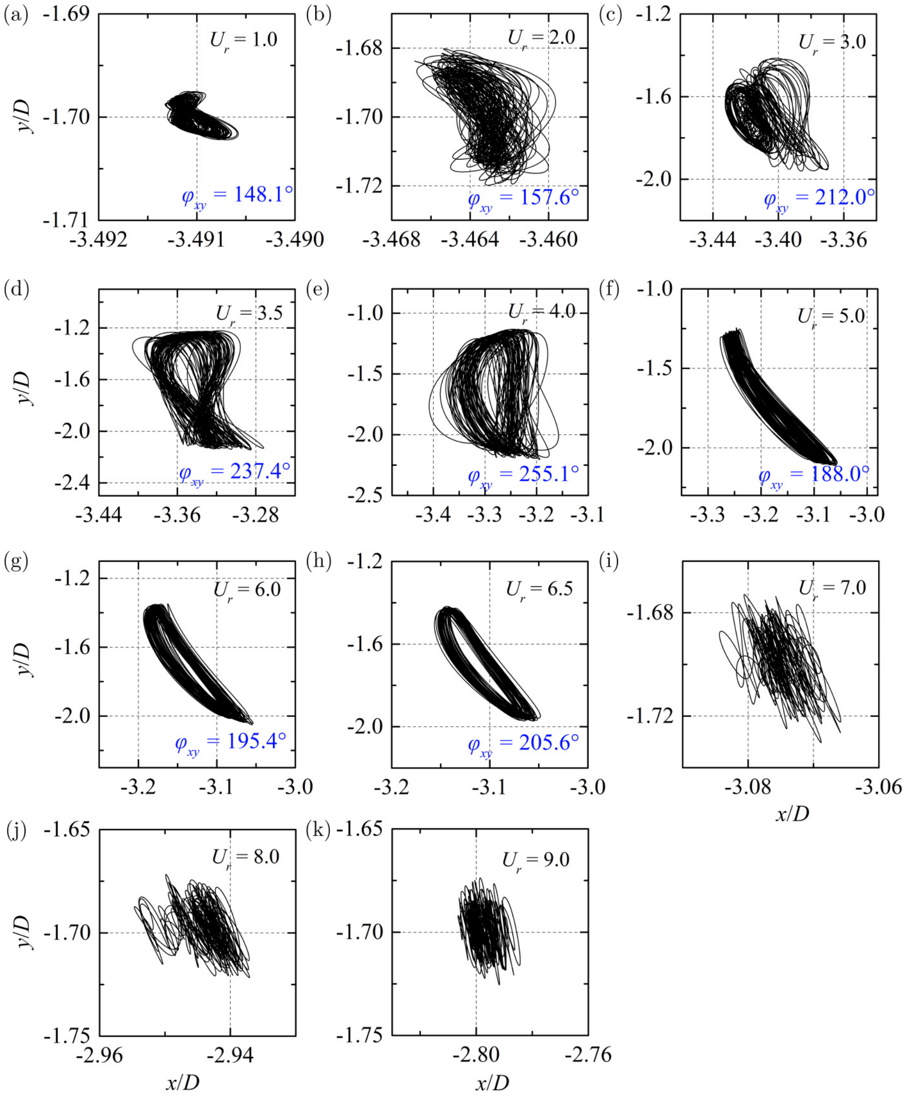

FIG. 6. Trajectories of the displacements in both directions in the VIV of a circular cylinder in proximity to a stationary wall at Re $= 500$ and $G/D = 0.8$. The phase lags between the displacements of both directions are presented. Due to the chaotic displacement at $U_r = 7.0$–9.0, no phase lags were obtained.

$U_r = 7.0$, where the phase lag between the lift and displacement changes from 0° to 180°, as shown later. As stated in [48], since the lift acts in the opposite direction to the body's motion, the response is significantly weakened. As indicated in Fig. 5(b), the phase jump occurs at the response transition from LB to DS-II, where f_y/f_n crosses 1.0 from a lower value. However, this is different from the positive-to-negative transition of $\bar{C}_{L,a}$, demarcating the upper and lower branches, in the VIV of an isolated circular cylinder in [48], and it can be attributed to the absence of the upper branch in this study due to the low-Re effect.

As shown in Fig. 8(b), the largest values of C_L' and $\bar{C}_L$ are not achieved at the same U_r. As a matter of fact, in the near-wall configuration, $\bar{C}_L$ depends significantly on the distance between the cylinder and the stationary wall [16]. Because of the near-wall suppression at $G/D = 0.8$, the gap-side shear layer of the cylinder is weaker than the freestream-side one. As a result, the pressure

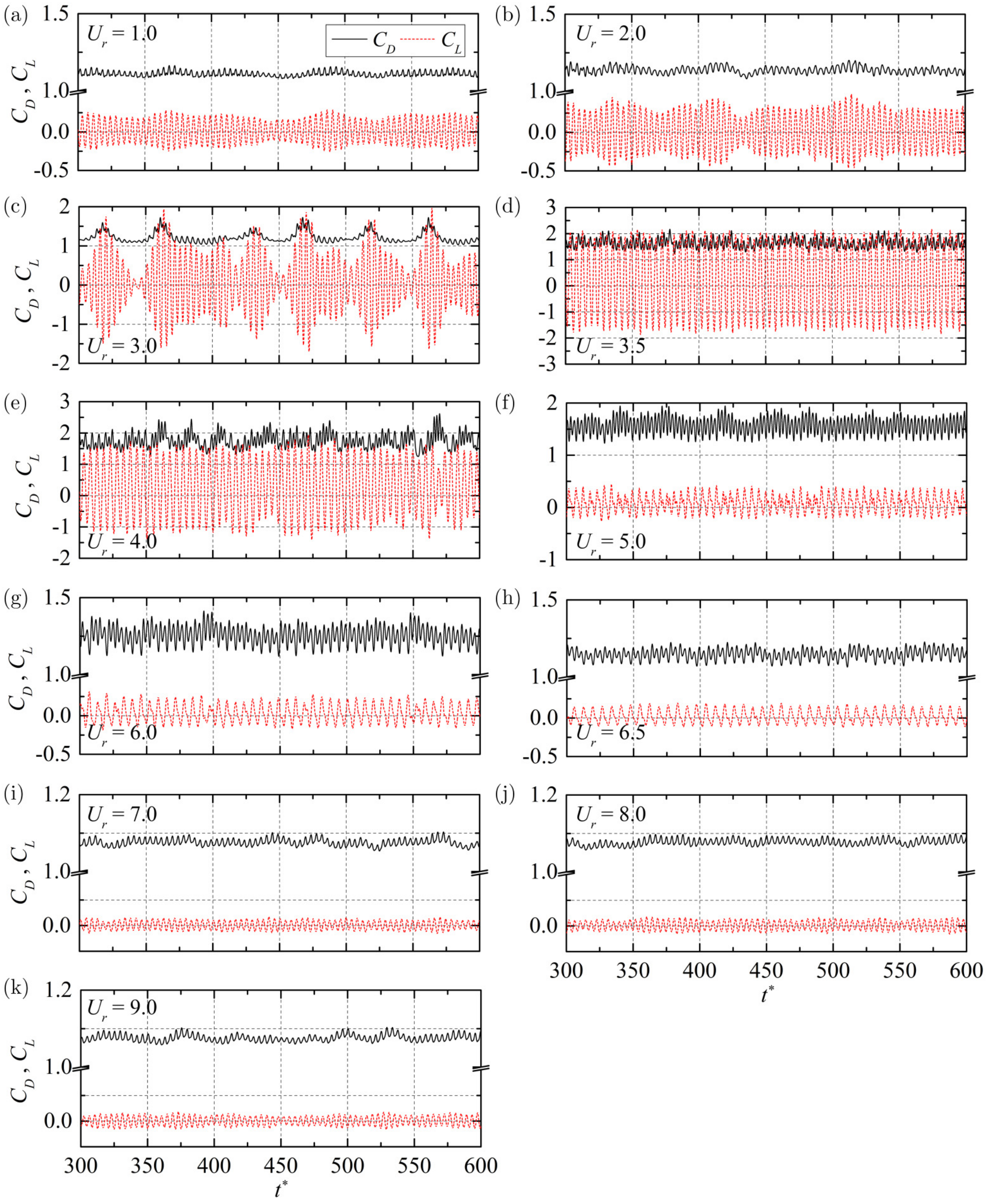

FIG. 7. Time histories of the drag and lift coefficients in the VIV of a circular cylinder in proximity to a stationary wall at Re $= 500$ and $G/D = 0.8$. Note that at $U_r = 6.5$, t^* ranges from 500 to 800.

is lower on the freestream side than that on the gap side, and $\bar{C}_L$ is positive. Moreover, the value of $\bar{C}_L$ is closely related with the vibration amplitude because large-amplitude vibrations further intensify the shear-layer strength difference and also the pressure difference on the two sides. As shown in Fig. 8(c), $\bar{C}_{L,v}$ is virtually zero in the whole U_r range, while $\bar{C}_{L,a}$ peaks at $U_r = 3.5$. As shown in the VIV results of an isolated cylinder [48], $\bar{C}_{L,a}$, which is related to the fluid inertia, peaks near the end of the initial branch and decreases at a larger U_r. This is also true for the near-wall VIV as indicated in Fig. 8(c). Because $\bar{C}_{L,a}$ dominates C'_L, the largest C'_L is obtained at $U_r = 3.5$ as $\bar{C}_{L,a}$.

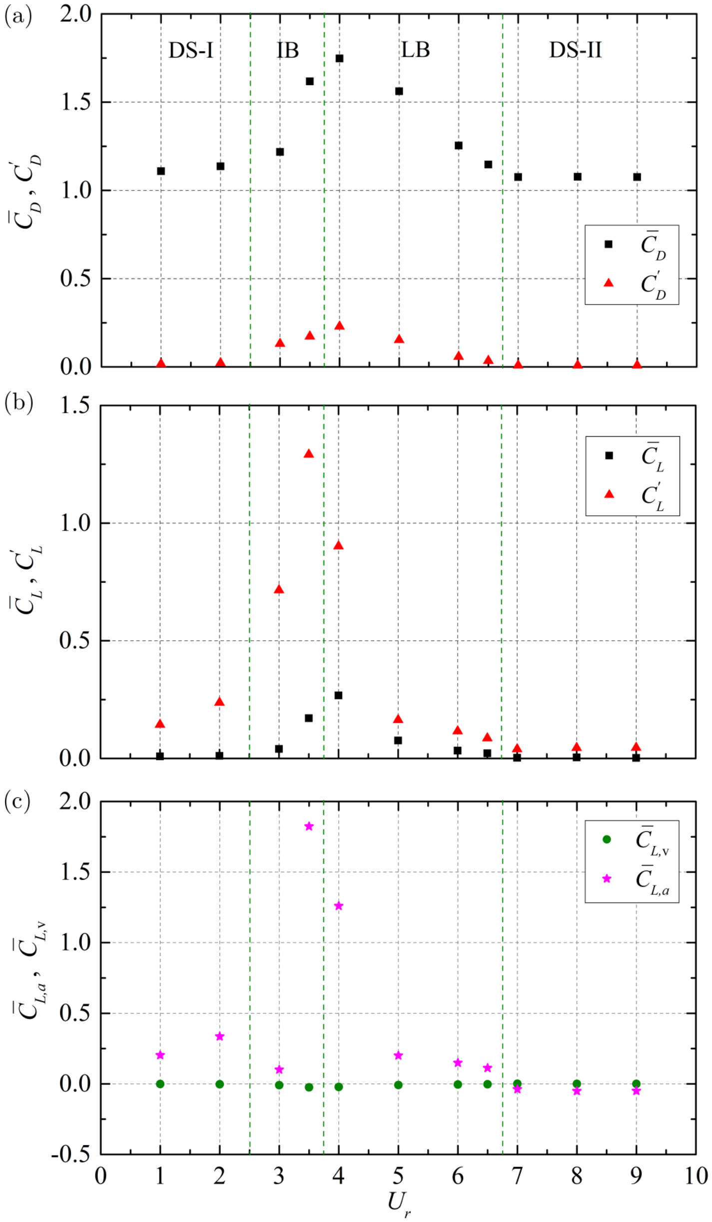

FIG. 8. Statistics of the drag and lift coefficients in the VIV of a circular cylinder in proximity to a stationary wall at $\mathrm{Re} = 500$ and $G/D = 0.8$: (a) for the drag coefficient, (b) for the lift coefficient, and (c) the decomposition of the lift coefficient.

Figure 9 displays the PSD results of the drag and lift coefficients at different reduced velocities. In the DS-I and DS-II, the dominant drag and lift frequencies are identical, with the same values as those of the stationary case. The second-harmonic frequency is observed in both DS-I and DS-II, and its amplitude is comparable to that of the fundamental frequency. In the IB, the dominant drag and lift frequencies become smaller than those of the stationary circular cylinder. With increasing U_r, the frequencies decrease slightly. Furthermore, corresponding to the beating phenomenon, two

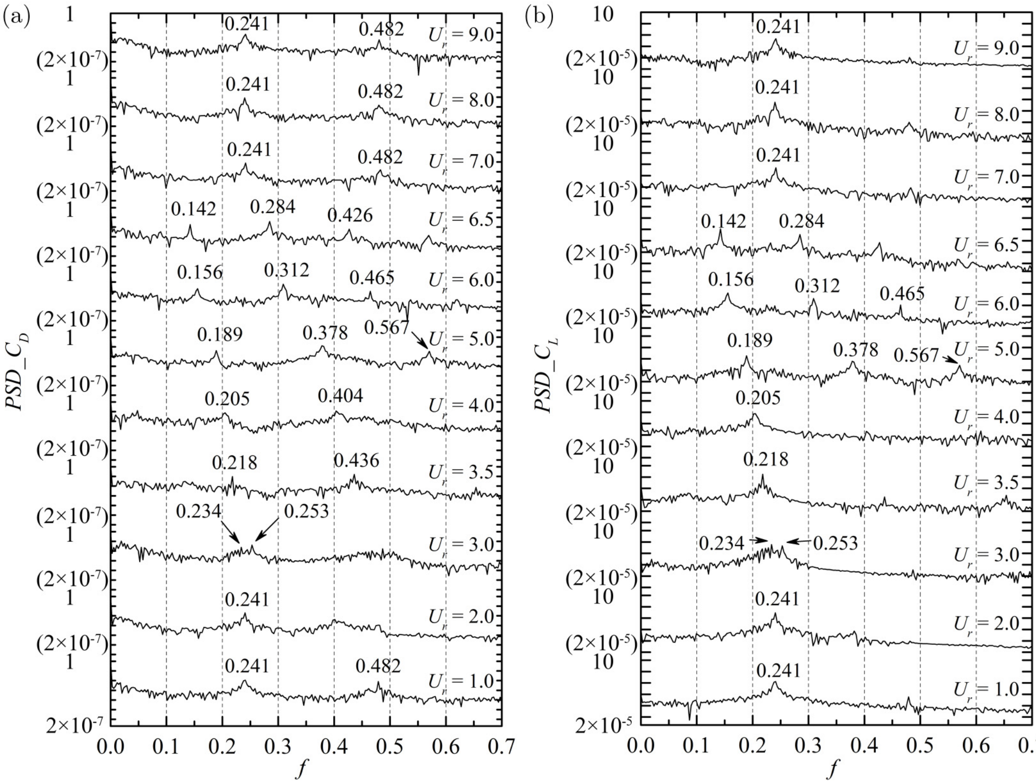

FIG. 9. PSD results of the drag and lift coefficients in the VIV of a circular cylinder in proximity to a stationary wall at Re = 500 and $G/D = 0.8$ (a) for the drag coefficient and (b) for the lift coefficient.

comparable frequencies are observed at $U_r = 3.0$ in both the drag and lift PSDs, and their values are identical to those of the displacement PSD. In the LB, the dominant drag and lift frequencies decrease with increasing U_r, with both the second and third harmonics existing. For the drag coefficient, the second harmonic has a larger amplitude than that of the fundamental frequency, while for the lift coefficient, the second harmonic appears only when $U_r > 4.0$.

C. Phase lags between the lift and displacement

Figure 10 shows the phase lag between the lift and displacement at different reduced velocities. It should be mentioned that only the fundamental components of the lift and displacement are applied to obtain the phase difference [49]. It is indicated that the phase lag is maintained at 0° in DS-I, IB, and LB, while a phase-lag jump from 0° to 180° occurs at the transition from LB to DS-II. A similar result has been reported in Chen *et al.* [16]. Contrastingly, in the VIV of an isolated cylinder at a similar Re, the phase-lag jump appears in the middle of LB [50]. Therefore, the proximity of a stationary wall leads to the delay of the phase-lag transition in the near-wall VIV [16].

D. Three-dimensionality of the wake structures

The wake three-dimensionality is discussed thoroughly from the aspects of instantaneous vortical structures, spanwise-averaged vorticity contours, statistics of the enstrophy, and plane vorticity contours. Figure 11 illustrates the instantaneous vortical structures at different reduced velocities when the cylinder is at the top. Generally, the vortical structures vary significantly with increasing

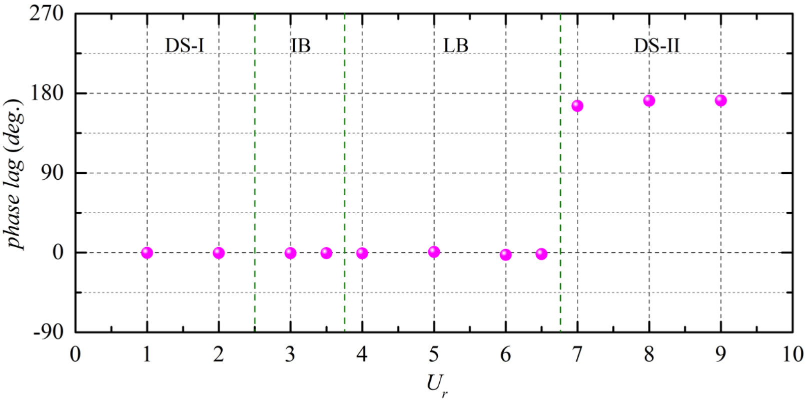

FIG. 10. Phase lag between the lift and displacement in the VIV of a circular cylinder in proximity to a stationary wall at $\mathrm{Re} = 500$ and $G/D = 0.8$.

U_r. As shown in Figs. 11(a) and 11(b), at $U_r = 1.0$, the gap-side vortex shedding of the cylinder is not synchronized along the span, with the middle part of the cylinder slightly leading the two ends. Although the shear layers along the span remain two-dimensional, the streamwise vortices appear but dissipate quickly. From the top view, the freestream-side vortices have higher strengths than the gap-side ones, therefore they can persist longer downstream [Fig. 11(b)]. At $U_r = 2.0$, the vortex shedding along the cylinder span becomes approximately synchronized [Figs. 11(c) and 11(d)]. Similar to that at $U_r = 1.0$, the stationary wall suppresses the development of the gap-side shear layer, and correspondingly, the freestream-side vortices are slightly stronger than those of the gap side.

As shown in Figs. 11(e)–11(h), the spanwise vortices at $U_r = 3.0$ and 3.5 are more irregular than those in the DS-I. As the transverse amplitude increases, the gap-side vortices display stronger interactions with the wall-generated boundary layer. As expected, the gap-side vortices become irregular at a shorter downstream compared to the freestream-side vortices. Moreover, comparing Figs. 11(e) and 11(g), the irregularity of the gap-side vortices is significantly intensified from $U_r =$ 3.0 to 3.5 due to the enlarged amplitude and the smaller distance to the stationary wall.

Similar to that in the IB, an obvious feature of the LB caused by the enlarged amplitude is that the coherence of the shear layer along the cylinder span becomes stronger. However, it should be noted that the increased amplitude does not lead to the vortices formed along the span being regular in the wake [Figs. 11(i)–11(p)]. In contrast, the vortical structures in the near wake become more chaotic with increasing transverse amplitude because of the stronger interactions with the boundary layer and the interferences by the vortices on both sides of the cylinder. The increased amplitude causes the cylinder to move closer to the stationary wall, and at the same time, the vortices on both sides of the cylinder interact at a closer distance downstream. Therefore, the spanwise vortices become wavy and scattered in the near wake, and the streamwise vortices dissipate quickly after the formation.

In the DS-II, the vibration amplitude reverts to approximately zero again. As depicted in Figs. 11(q)–11(v), the vortical structures at $U_r = 7.0$–9.0 are almost the same. As indicated in Figs. 11(r), 11(t), and 11(v), the freestream-side vortices along the cylinder span are not synchronized, and the dislocations persist as the vortices move downstream. Due to the stabilizing role of the gap flow, the gap-side vortices along the cylinder span are more synchronized [Figs. 11(q), 11(s), and 11(u)]. The gap-side streamwise vortices have a hairpin-like shape and are carried by the gap flow deflecting upward, with the heads slightly higher than the tails. Because of the interactions with the freestream-side vortices, these hairpin vortices dissipate in the near wake.

From the above discussion, we observe that the vortical structures show obvious three-dimensional features. In the DS-I and DS-II where the vibration amplitude is approximately zero,

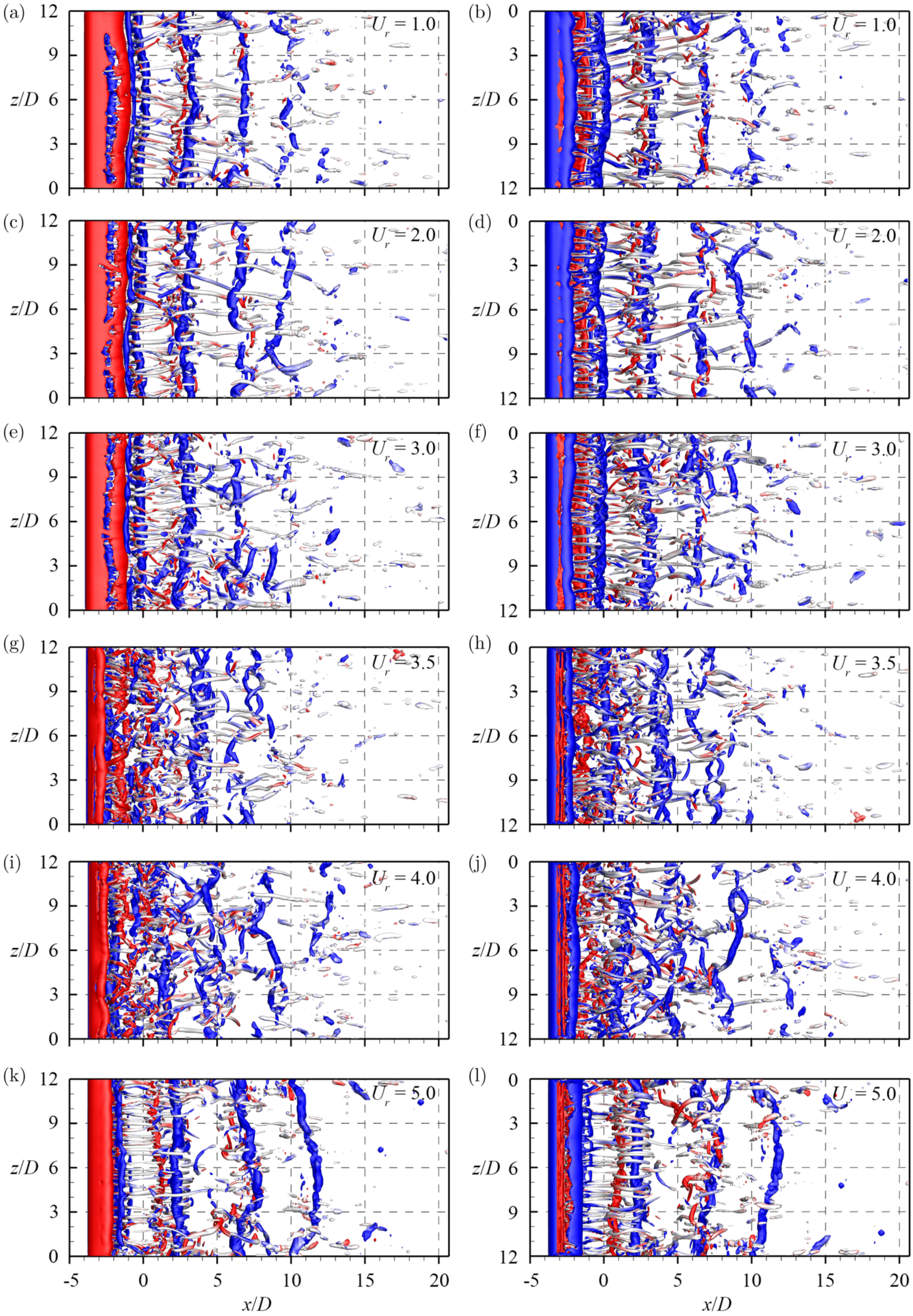

FIG. 11. Instantaneous vortical structures represented by the isosurface at $\lambda_2 = -1$ for the VIV of a circular cylinder in proximity to a stationary wall at $\mathrm{Re} = 500$ and $G/D = 0.8$. Colors denote the nondimensional Z-vorticity in the range of -2 to 2 with an increment of 0.2, with blue and red representing the negative and positive z-vorticity, respectively. The left column shows the wake viewed from the bottom, while the right column shows the wake viewed from the top. The instant that the cylinder is at the highest position is selected for each U_r case.

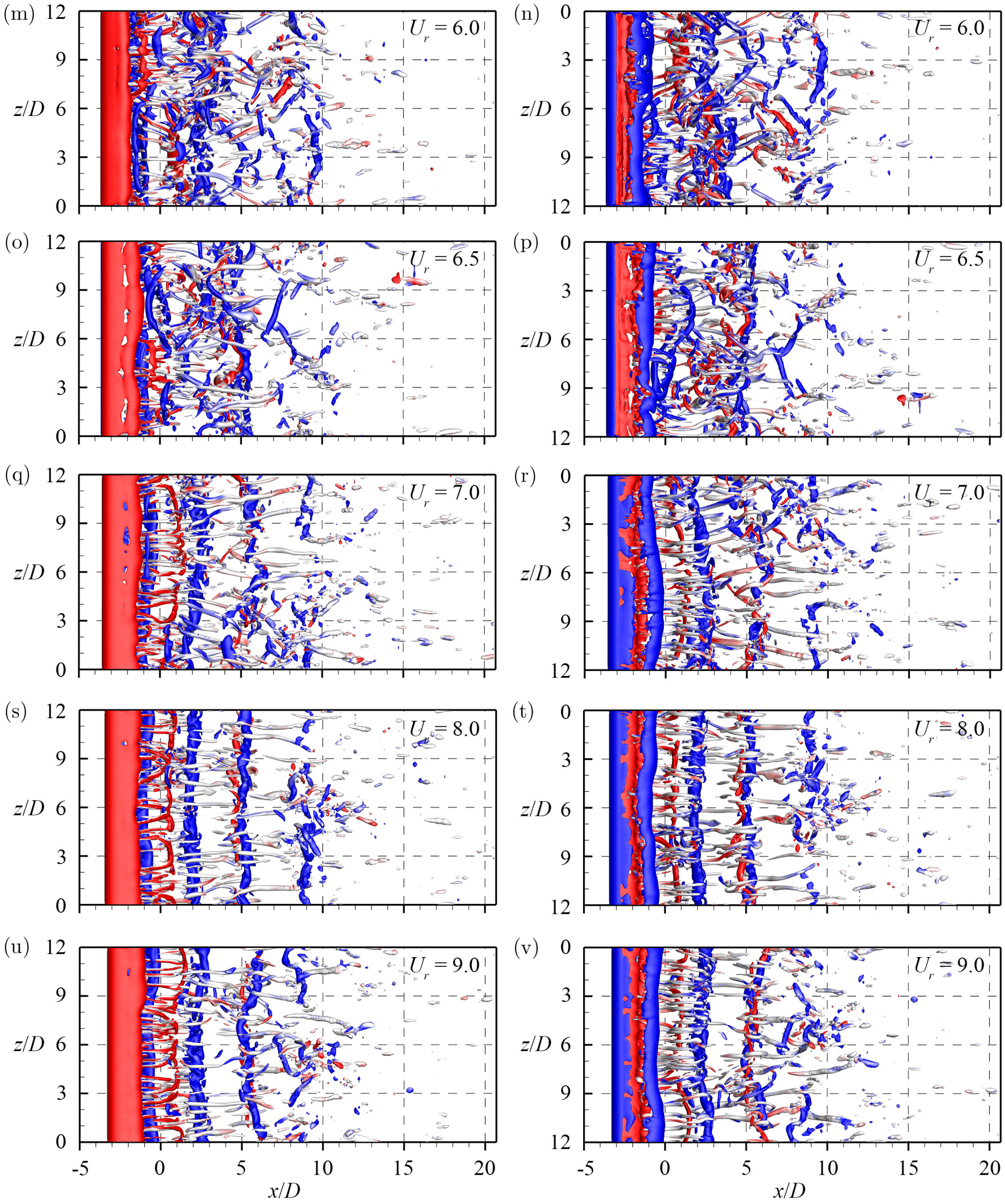

FIG. 11. (*Continued.*)

the vortex shedding dislocations along the span are evident. However, in the IB and LB, because of the enlarged vibration amplitude, the vortex shedding along the cylinder span becomes stronger and more synchronized. As the cylinder moves closer to the stationary wall, the interactions with the boundary layer are intensified and, therefore, the gap-side vortices show more irregularity while quicker dissipation. In addition, the enlarged vibration amplitude also results in stronger interferences between the vortices shed from the two sides of the cylinder, giving rise to the increased irregularity of the freestream-side vortices.

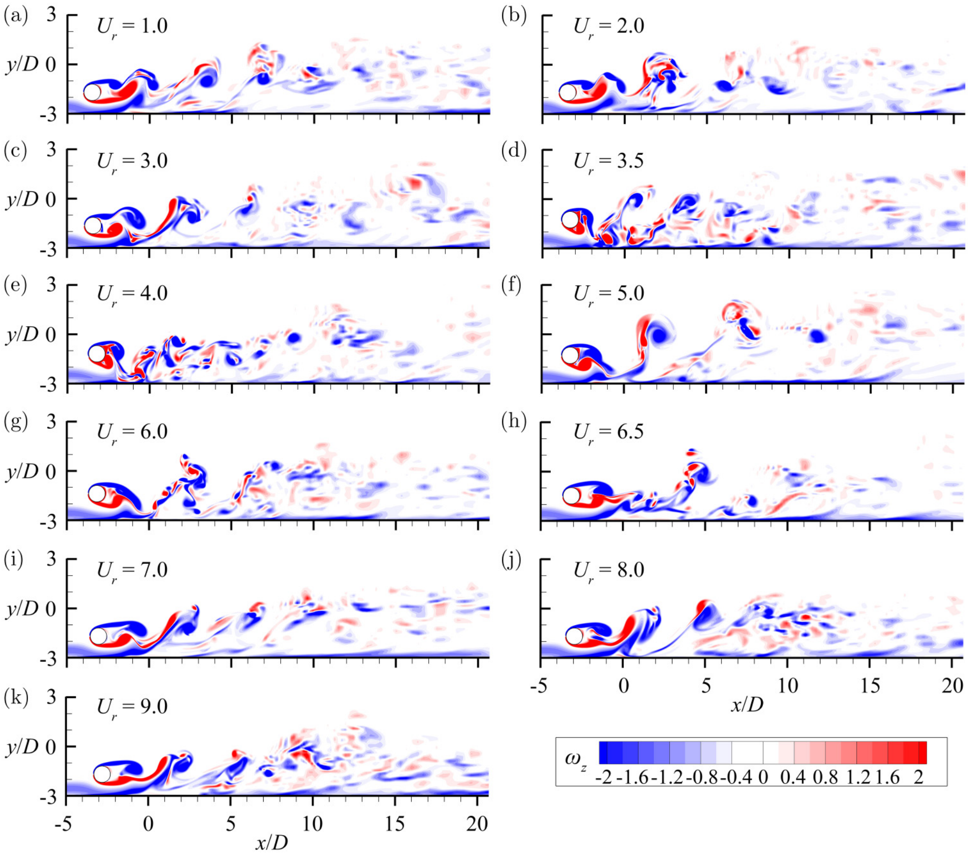

FIG. 12. Spanwise-averaged z-vorticity contours in the VIV of a circular cylinder in proximity to a stationary wall at $U_r = 1.0$–9.0. The instants are the same as those in Fig. 11 when the cylinder is at the highest position.

To further explain the interactions of the vibrating cylinder and the wall-generated boundary layer, the spanwise-averaged z-vorticity contours are presented in Fig. 12. Generally, in a vibration cycle, one vortex is shed from each side of the cylinder, signifying the typical 2S mode for all the simulated U_r. As shown in Figs. 12(a) and 12(b), when the cylinder reaches the highest, the vortices are only separated from the freestream side of the cylinder, and the gap-side shear layer plays a cutoff role in the formation of the freestream-side vortices. Accompanied with the uplifted gap flow, the gap-side vortices are deflected upward and interact with the freestream-side vortices. As a result, the vortex street dissipates quickly in the wake.

In the IB and LB, the vibration amplitudes are much larger than those in the DS. An obvious difference is that the vortices form closer to the cylinder base [Figs. 12(c)–12(h)]. Moreover, in these two branches, the cylinder moves closer to the stationary wall when it reaches the lowest position, and correspondingly, the interactions of the vortices with the boundary layer are also stronger. As indicated in Figs. 12(d) and 12(e), the vortices shed from the cylinder move directly towards the wall and exhibit direct interactions with the wall-generated boundary layer, and then the vortices break down into small parts in the near wake. Wrinkles form in the boundary layer when the vortices move slightly closer to the wall [Figs. 12(c)–12(h)].

Because of the change of the lift-displacement phase lag from 0° to 180°, a contrastingly different vortex shedding is observed in the DS-I and DS-II. Comparing Figs. 12(a) and 12(b) and Figs. 12(i)–12(k), it can be observed that when the cylinder reaches the top, the freestream-side vortices have

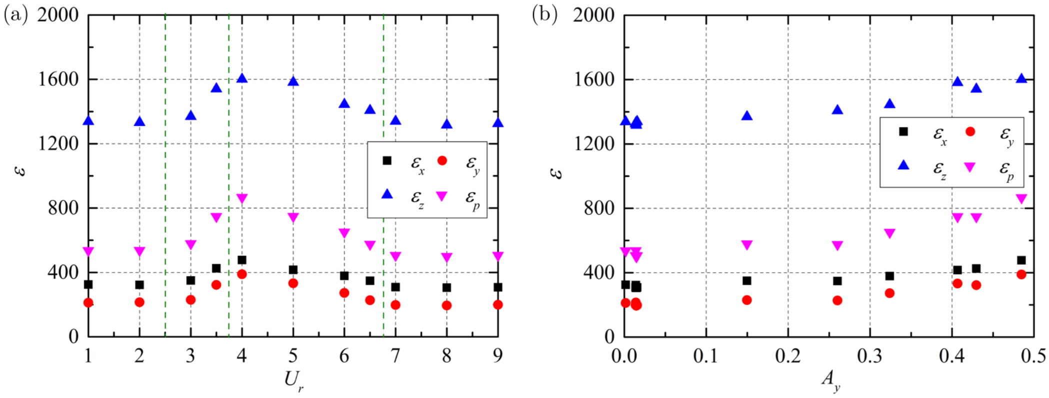

FIG. 13. Statistics of the enstrophies in the VIV of a circular cylinder in proximity to a stationary wall with the reduced velocity and the vibration amplitude at Re = 500 and $G/D = 0.8$.

just separated from the cylinder in the DS-II, while the gap-side vortices have separated from the cylinder in the DS-I.

The three-dimensionality of the wake can be reflected by enstrophies [51–55]. Here, we investigate the enstrophies to analyze the variations in the vorticity of different rotations [51,56,57]. The enstrophies (ε_x, ε_y, ε_p, and ε_z) are defined as

$$\varepsilon_x = \frac{1}{2}\int_V \omega_x^2 dV, \tag{5}$$

$$\varepsilon_y = \frac{1}{2}\int_V \omega_y^2 dV, \tag{6}$$

$$\varepsilon_p = \frac{1}{2}\int_V (\omega_x^2 + \omega_y^2) dV, \tag{7}$$

$$\varepsilon_z = \frac{1}{2}\int_V \omega_z^2 dV, \tag{8}$$

where V denotes the volume of the computational domain, and ω_x, ω_y, and ω_z denote the nondimensional vorticities defined as $\omega_x = \frac{D}{U_\infty}(\frac{\partial w}{\partial y} - \frac{\partial v}{\partial z})$, $\omega_y = \frac{D}{U_\infty}(\frac{\partial u}{\partial z} - \frac{\partial w}{\partial y})$, and $\omega_z = \frac{D}{U_\infty}(\frac{\partial v}{\partial x} - \frac{\partial u}{\partial y})$, respectively. Figure 13 depicts the variations in the enstrophies, including ε_x, ε_y, ε_z and ε_p, with U_r and A_y. As shown in Fig. 13(a), the enstrophies follow the same trend, which is expected given the fact that the plane vorticities, including ε_x, ε_y, and ε_p, are caused by the instability of the spanwise vortices [58]. In detail, the enstrophies are approximately constant in the DS-I and DS-II, while in the IB and LB, they first increase and then decrease with increasing U_r. As illustrated in Fig. 13(a), in the simulated U_r range, ε_x is slightly larger than ε_y, while ε_z is approximately two times larger than ε_p. However, as displayed in Fig. 13(b), the enstrophies show an approximately linear increase with increasing A_y, which indicates that the vorticities of different rotations are strongly dependent on the vibration amplitude.

Figure 14 presents the spanwise-averaged secondary enstrophy (ε_p) contours when the cylinder is at the highest position. In the DS-I, ε_p mainly appear at the freestream side of the wake, consistent with the distribution of the spanwise vortices [see Figs. 11(a) and 11(b) and Figs. 12(a) and 12(b)]. However, because of the change of the vortex shedding timing, ε_p in the DS-II mainly appear downstream of the cylinder base [Figs. 14(i)–14(k)]. In IB and LB, ε_p emerge at a location closer to the cylinder base, and their strengths are stronger than those of the DS because of the increased amplitude. In the DS, the amplitudes are insignificant, and ε_p saturate at approximately

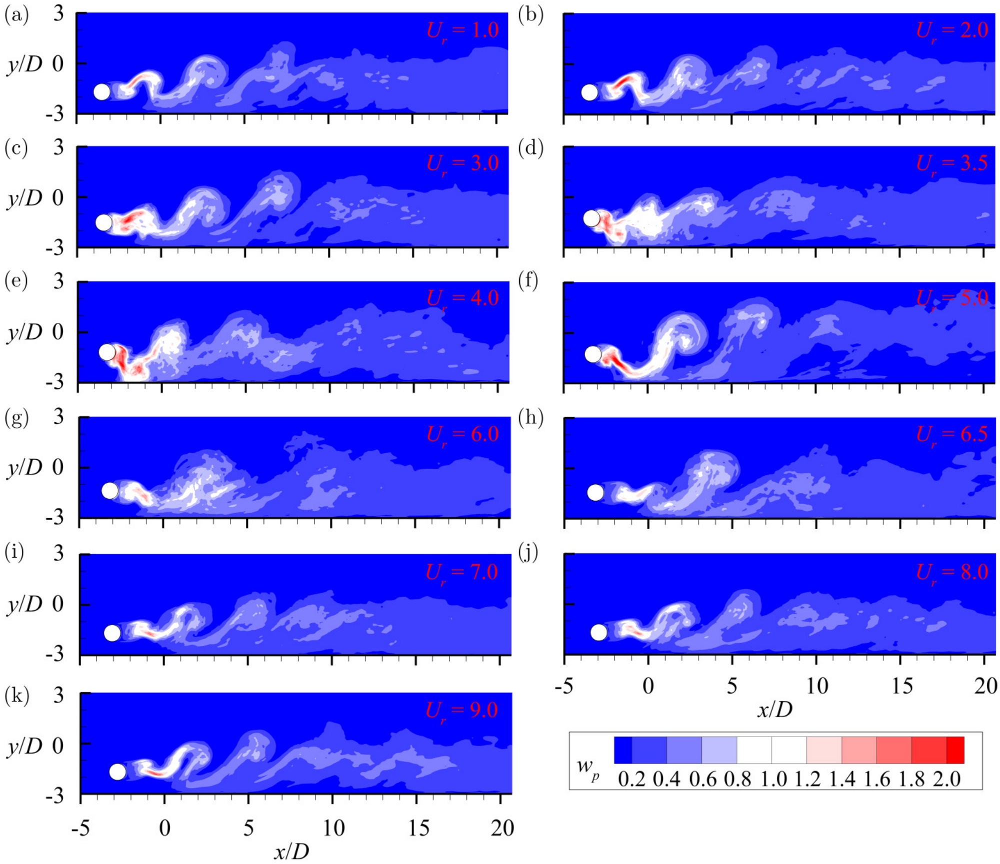

FIG. 14. Spanwise-averaged secondary enstrophy (ε_p) contour in the VIV of a circular cylinder in proximity to a stationary wall at Re = 500 and $G/D = 0.8$. For each U_r case, the instant that the cylinder is at the highest position is applied.

$1D$ downstream of the cylinder. This agrees well with that of an isolated stationary cylinder [59]. In the near-wall configuration, because of the upward-deflected gap flow, ε_p move upward slightly, consistent with the movement of the spanwise vortices.

E. Statistics of the gap flow

The instantaneous streamwise velocity U_g spatially averaged over the gap is defined as $U_g = \frac{1}{2.5D+y_c}\int_0^{12D}\int_{-3D}^{y_c-0.5D} u\,dydz$, where u is the streamwise velocity and y_c is the instantaneous location of the cylinder center. Figure 15 indicates the variations in the temporal mean $\bar{U}_g$ and fluctuation $\bar{U}_{g,\mathrm{rms}}$ of U_g at different reduced velocities. As shown in Fig. 15(a), $\bar{U}_g$ remains almost constant with U_r except at $U_r = 3.5$–4.0, suggesting the negligible effects of cylinder oscillation on the averaged gap flow velocity. Furthermore, the $\bar{U}_g$ variation with the displacement shift ($\bar{y}/D$) illustrated in Fig. 15(c) clearly indicates that $\bar{U}_g$ depends closely on the time-averaged gap space ($=G/D + \bar{y}/D$). When $\bar{y}/D$ is larger than 0.016, $\bar{U}_g$ shows a significant decrease, signifying that a small increase in the time-averaged gap can lead to a remarkable drop in $\bar{U}_g$. The root-mean-square (rms) streamwise velocity of the gap flow has contrastingly different behavior. As shown in Fig. 15(b), in the DS, $\bar{U}_{g,\mathrm{rms}}$ is constant at a small value, but it increases in the IB and decreases in the LB. This trend is similar to that of the amplitude. Furthermore, the linear increase of $\bar{U}_{g,\mathrm{rms}}$ with the transverse

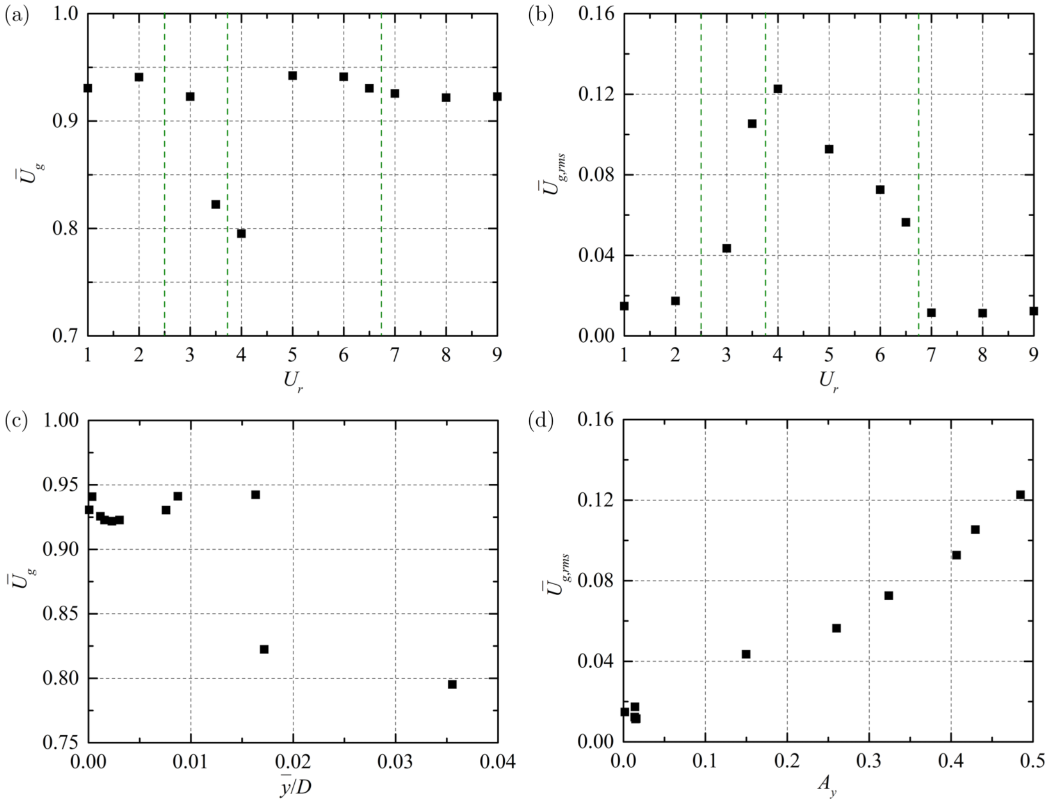

FIG. 15. Time- and spanwise-averaged gap flow velocities in the VIV of a circular cylinder at Re = 500 and $G/D = 0.8$: (a) mean streamwise velocity and (b) rms streamwise velocity with U_r; (c) mean streamwise velocity with the displacement shift; (d) rms streamwise velocity with the amplitude.

amplitude presented in Fig. 15(d) signifies that $\bar{U}_{g,\mathrm{rms}}$ depends strongly on the amplitude. Therefore, it is clear that $\bar{U}_g$ and $\bar{U}_{g,\mathrm{rms}}$ can be the appropriate metrics for the mean gap and vibration amplitude, respectively.

F. Time-averaged flow fields

Figure 16 shows the time- and spanwise-averaged streamwise velocity fields at different reduced velocities. As displayed in Figs. 16(a), 16(c), 16(e), and 16(g), there is an obvious recirculation bubble for each case in the range of $U_r = 1.0$–3.5, and as a result of the upward deflected gap flow, these bubbles are slightly upward. With increasing vibration amplitude, the distance between the bubble and cylinder decreases gradually. In contrast, as presented in Figs. 16(b) and 16(d), the fluctuating streamwise velocities in the DS-I mainly occur in the near wake, with lower strength. In the IB, the fluctuating streamwise velocity becomes larger, particularly around the cylinder. In the DS-II, the fluctuating streamwise velocity is comparable to that in the DS-I, but it appears slightly farther downstream [Figs. 16(q)–16(v)]. In the LB, the negative velocity region at the bottom of the cylinder increases gradually with increasing U_r or decreasing amplitude [Figs. 16(i), 16(k), 16(m), and 16(o)]. As indicated in Figs. 12(e)–12(h), when the amplitude is large, the shear layers of the cylinder exhibit stronger fluctuations at a shorter distance downstream, and the bubbles shrink. As the amplitude decreases, the fluctuations occur at a farther distance downstream, and correspondingly, the negative region is enlarged.

Figure 17 illustrates the time-averaged transverse velocity fields at different reduced velocities. The mean transverse velocity becomes large at three distinct regions, i.e., two at the freestream

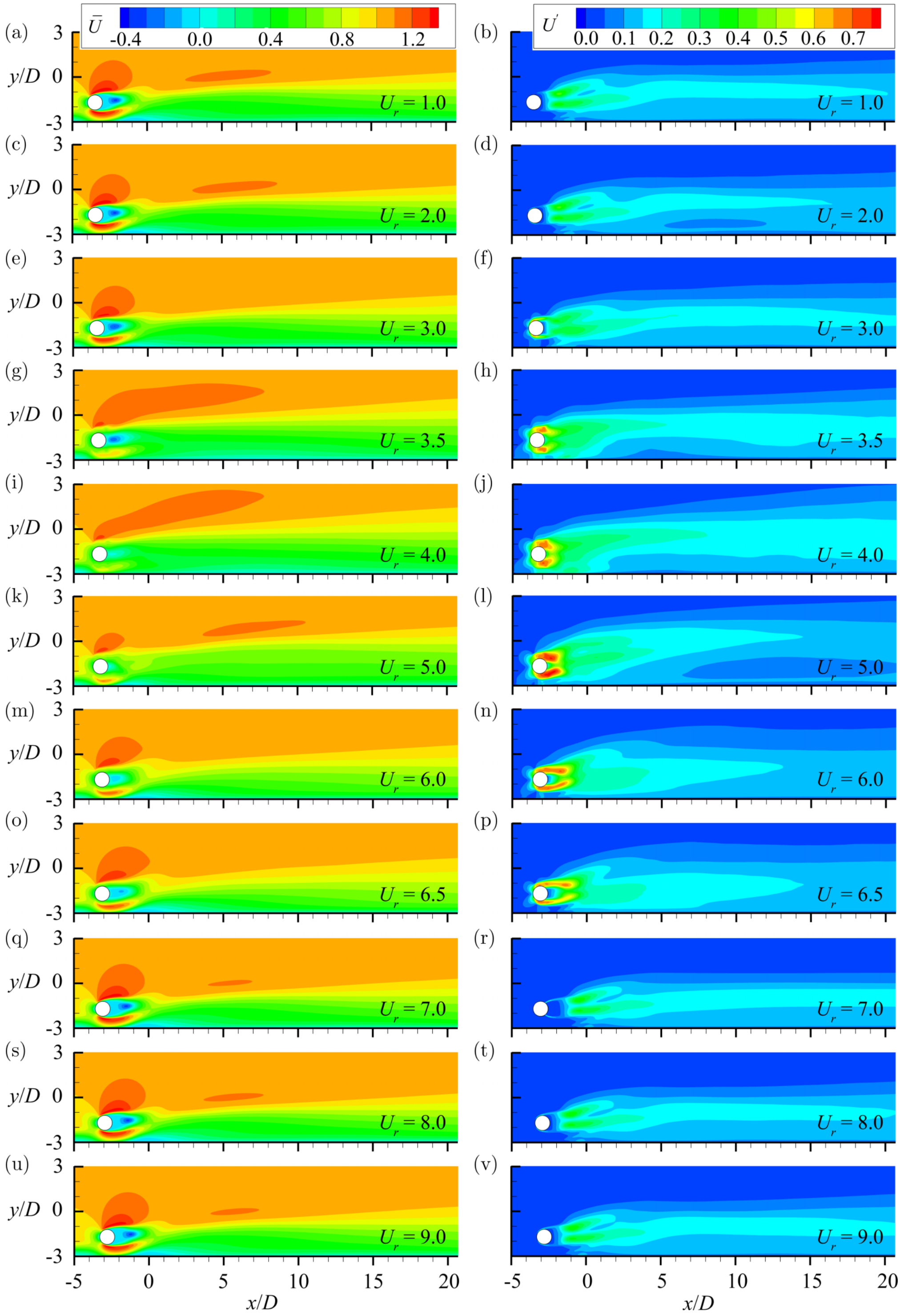

FIG. 16. Streamwise velocities in the VIV of a circular cylinder in proximity to the stationary wall at Re = 500 and $G/D = 0.8$. The left and right columns represent the mean and fluctuating velocities, respectively.

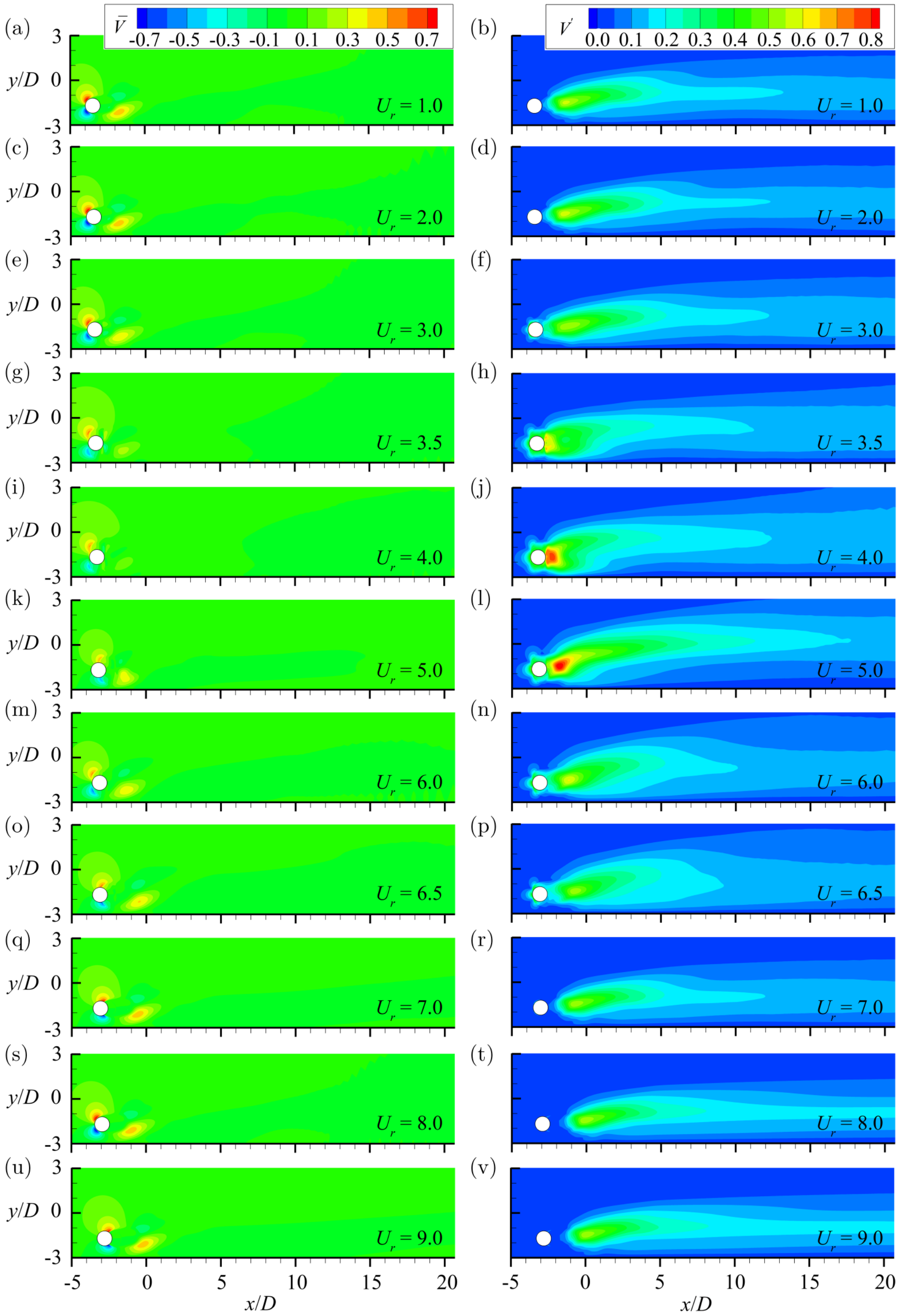

FIG. 17. Transverse velocities in the VIV of a circular cylinder in proximity to a stationary wall at $\mathrm{Re} = 500$ and $G/D = 0.8$. The left and right columns represent the mean and fluctuating velocities, respectively.

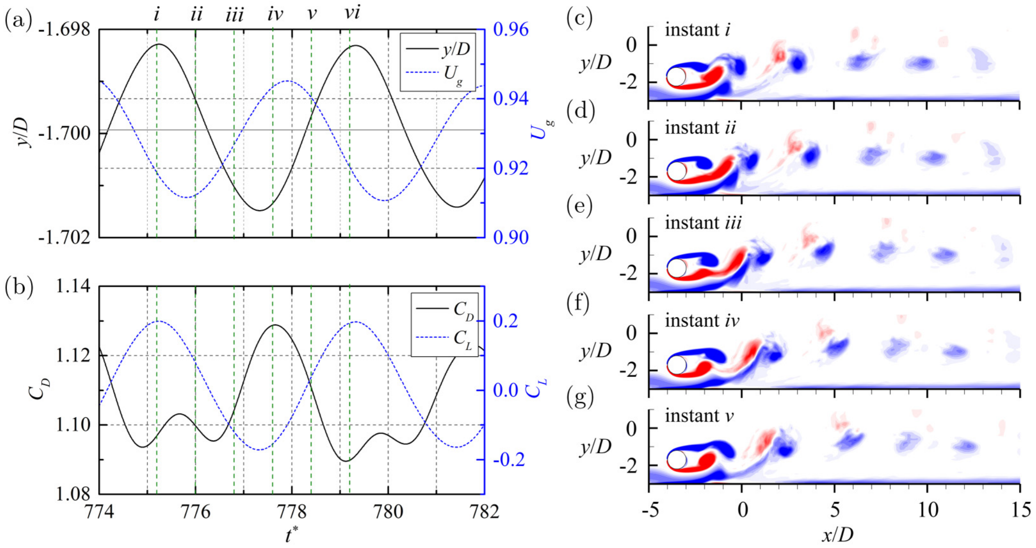

FIG. 18. Time histories of (a), (b) the transverse displacement, spanwise-averaged gap flow velocity, drag, and lift coefficients, and (c)–(g) vorticity contours of one period in the VIV of a circular cylinder in proximity to the stationary wall at $U_r = 1.0$ (DS-I). Because the vorticity contour at instant *vi* is the same as that at instant *i*, it is not presented here. The color bar for the contour plots is the same as that of Fig. 12.

and gap sides of the cylinder, and one slightly downstream of the gap. The former two are closely related to the movement of the cylinder, while the latter is caused by the upward motion of the wall-generated boundary layer. Generally, the three regions in the DS are more noticeable than those in the IB and LB. As for the fluctuating transverse velocity, it appears mainly at the base of the cylinder and becomes larger in the IB and LB. Corresponding to the larger vortex formation region, the fluctuating transverse velocity in the DS-I begins at a slightly longer distance downstream than that in the DS-II.

G. Flow physics of different branches

In the above sections, the amplitudes, fluid forces, spectral frequencies, wake three-dimensionality, and statistics of the gap flow are examined thoroughly. In this section, the flow physics of each branch associated with the instantaneous vorticity contours, time histories of the displacement, gap flow velocity, and drag and lift coefficients are elucidated. In each region, one reduced velocity, i.e., $U_r = 1.0$ (DS-I), 3.0 (IB), 4.0 (LB), and 8.0 (DS-II), is selected.

As shown in Figs. 18(a) and 18(c), when the cylinder moves back from the top in the DS-I, the freestream-side vortex has just separated from the cylinder, while the gap-side shear layer is developing. Attracted by the freestream-side vortex, the boundary layer of the wall moves upward and will exhibit direct interactions later. From Fig. 18(a), we can further observe that although the cylinder is at the top, the gap flow velocity decreases when the cylinder moves toward the stationary wall (from instant *i* to *ii*). Because the displacement of the cylinder is negligible, the variation in the gap flow is determined by the vortex shedding. When the cylinder moves towards the wall, both the gap-side shear layer of the cylinder and the wall-generated boundary layer develop; therefore, the flow through the gap is delayed. In addition, when the cylinder is at the top, the lift coefficient reaches its peak, suggesting an in-phase behavior between the displacement and lift coefficient, while the drag coefficient has just reached the lowest value [Fig. 18(b)].

As depicted in Figs. 18(a), 18(d), and 18(e), when the cylinder moves towards the bottom (from instant *ii* to *iii*), the gap-side shear layer of the cylinder develops, while the boundary layer merges

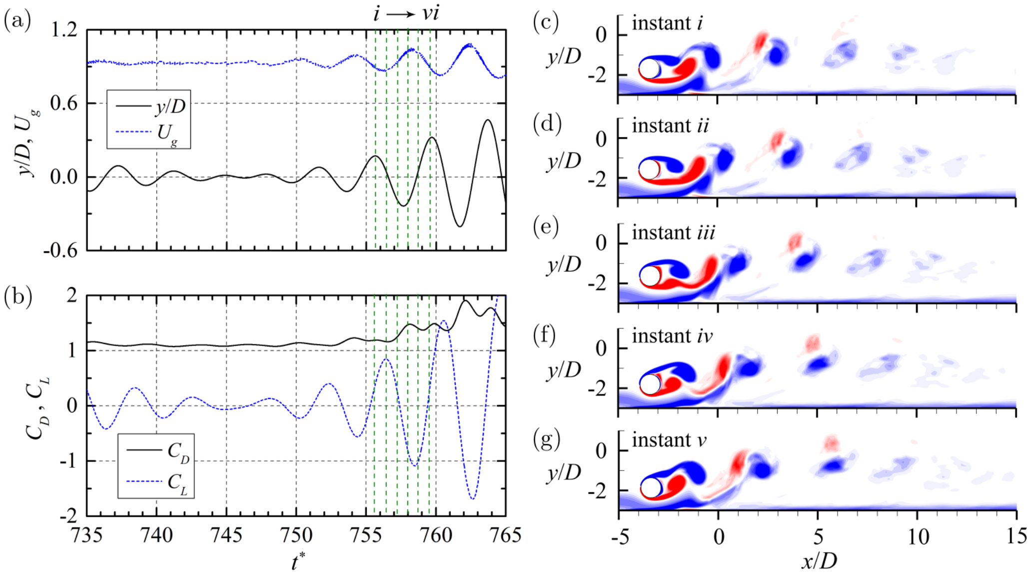

FIG. 19. Time histories of (a), (b) the transverse displacement, spanwise-averaged gap flow velocity, drag, and lift coefficients, and (c)–(g) vorticity contours of one period in the VIV of a circular cylinder in proximity to a stationary wall at $U_r = 3.0$ (IB). Instants from i to vi are marked in (a), (b) from left to right. Because the vorticity contour at instant vi is similar to that at instant i, it is not presented here. The color bar for the contour plots is the same as that of Fig. 12.

with the freestream-side vortex of the cylinder. Due to the coalescence of the freestream-side vortex with the boundary layer, the gap-side vortex moves upward. Furthermore, because of the development of the gap-side shear layer, the lift coefficient decreases monotonically, while the drag coefficient only displays a small variation [Fig. 18(b)]. When the cylinder moves toward the top from the bottom (from instant iv to vi), the gap-side vortex has just separated from the cylinder; it then moves toward the freestream side of the negative vortex [Figs. 18(a), 18(f), and 18(g)]. The vortices from both sides of the cylinder pair in the near wake and move downstream abreast. However, because of the low strength, the gap-side vortex dissipates more quickly than the freestream-side vortex. From instant iv to vi, the gap flow velocity first increases and then decreases, with the peak occurring at the middle of instants iv and v. That is, the gap flow velocity reaches its peak at the instant when the gap-side vortex is shed from the cylinder. Furthermore, from instant iv to vi, the lift coefficient increases monotonically while the drag coefficient decreases from the peak [Fig. 18(b)]. At instant iv, the gap-side vortex has just separated from the cylinder and the remaining shear layer comes closer to the cylinder because of the pushing effects of the freestream-side shear layer, resulting in the largest drag.

In the IB, the displacement at $U_r = 3.0$ is similar to beating, and its fluctuation varies. When the fluctuation is approximately zero, the vortex dynamics are the same as those in the DS-I. Therefore, in this branch, only the vortex dynamics of the transition from small to large fluctuations are explored. As shown in Fig. 19, although the displacement is remarkably larger than that in the DS-I, the vortex dynamics and variations in the drag and lift coefficients and gap flow velocity are similar to those in the DS-I. As displayed in Figs. 19(a) and 19(c), when the cylinder is at the top (instant i), the freestream-side vortex has just separated from the cylinder, and because of the attraction of the freestream-side vortex of the cylinder, the boundary layer moves upwards gradually. At this instant, the gap flow velocity is approaching the lowest value. A slight difference from that in the DS-I is that when the cylinder is at the top, the lift coefficient does not reach the peak, which is mainly caused by the presence of the beating component [Fig. 19(b)]. As the cylinder moves toward

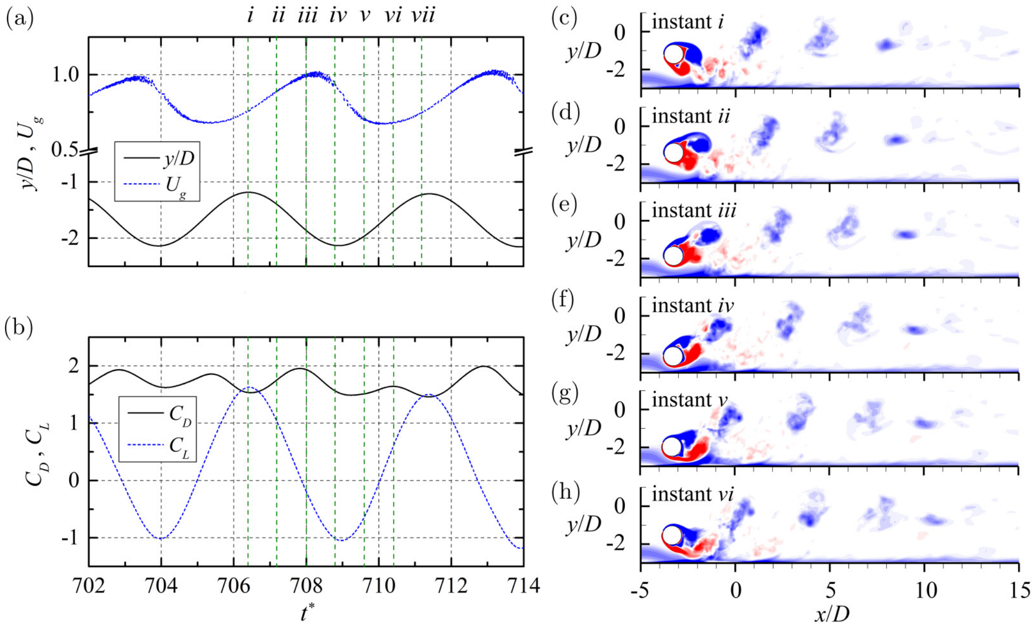

FIG. 20. Time histories of (a), (b) the transverse displacement, spanwise-averaged gap flow velocity, drag, and lift coefficients, and (c)–(g) vorticity contours of one period in the VIV of a circular cylinder in proximity to the stationary wall at $U_r = 4.0$ (LB). Because the vorticity contour at instant *vii* is the same as that at instant *i*, it is not presented here. The color bar for the contour plots is the same as that of Fig. 12.

the bottom, the gap-side shear layer of the cylinder develops, and the boundary layer merges with the freestream-side vortex [Figs. 19(a), 19(d), and 19(e)]. In this process (from instant *ii* to *iii*), the gap flow reaches the lowest value at instant *ii* when the cylinder is around the mean position. In contrast, the lift coefficient reaches its peak at instant *ii* and afterward decreases [Fig. 19(b)].

When the cylinder moves towards the top (from instant *iv* to *vi*), the gap-side vortex of the cylinder pairs with the coalesced vortex, and they move downstream abreast, with the positive one at the freestream side [Figs. 19(a), 19(f), and 19(g)]. Similar to that in the DS-I, the vortex from the gap side of the cylinder dissipates more quickly. In this half-period, the gap flow velocity reaches its peak when the cylinder has just passed through the bottom and begins to decrease when the cylinder is close to the mean position [Fig. 19(a)]. Furthermore, as the fluctuation of the displacement increases, the drag coefficient increases as well. Compared to the drag coefficient, the fluctuating lift increases more significantly. When the displacement has a larger fluctuation, vortices form in the closer wake, and correspondingly, both the drag and lift coefficients become larger. In addition, because of the large amplitude, the vortices in the IB become stronger than those in the DS-I.

In the LB, the amplitude is much larger. As shown in Figs. 20(a) and 20(b), the time histories of the displacement, gap flow velocity, and drag and lift coefficients exhibit significant variations within one period. When the cylinder is at the top, the shear layers surround the cylinder closely, with the freestream side being slightly stronger than the gap side [Fig. 20(c)]. Furthermore, the vortex from the gap side of the cylinder collides with the wall and breaks down into small parts. Therefore, no positive vortices are observed in the wake. When the cylinder moves toward the bottom (from instant *ii* to *iv*), the freestream-side shear layer saturates gradually and rolls up into a vortex at instant *iii* before the cylinder reaches the bottom [Figs. 20(a) and 20(d)–20(f)]. Meanwhile, the gap-side shear layer closely envelopes the bottom side of the cylinder. Therefore, in this process, the drag coefficient reaches the peak at instant *iii* and afterward decreases, whereas the lift coefficient decreases monotonically to the lowest value [Fig. 20(b)]. Furthermore, because

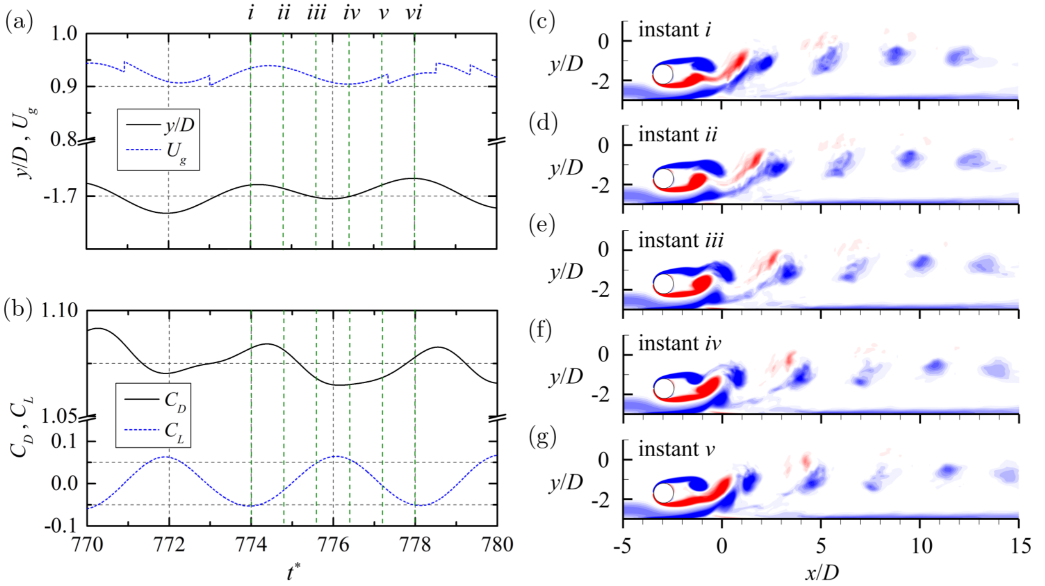

FIG. 21. Time histories of the (a), (b) transverse displacement, spanwise-averaged gap flow velocity, drag, and lift coefficients, and (c)–(g) vorticity contours of one period in the VIV of a circular cylinder in proximity to the stationary wall at $U_r = 8.0$ (DS-II). Because the vorticity contour at instant vi is similar to that at instant i, it is not presented here. The color bar for the contour plots is the same as that of Fig. 12.

the gap-side shear layer moves toward the cylinder bottom, more space appears for the passage of the gap flow, and therefore, the gap flow velocity increases until instant *iii* [Fig. 20(a)]. When the cylinder is sufficiently close to the stationary wall, the gap flow velocity decreases.

When the cylinder moves toward the top from the bottom (from instant *iv* to *vii*), the gap-side shear layer develops [Figs. 20(a), 20(g), and 20(h)]. However, because the cylinder is close to the stationary wall, the gap-side shear layer crashes into the wall before it is completely separated from the cylinder. Consequently, the gap-side shear layer splits into small vortices, dissipating quickly. In this half period, the gap flow velocity first decreases and then increases, with the lowest value appearing at instant vi, where the cylinder is near the mean position [Fig. 20(a)]. Concerning the forces, the drag coefficient exhibits a relatively small variation, whereas the lift coefficient increases gradually, which is related to the development of the freestream-side shear layer.

In the DS-II, the fluctuations in the displacement revert to negligible values, and correspondingly, the drag and lift coefficients display small variations [Figs. 21(a) and 21(b)]. As expected, the gap flow velocity varies slightly. Because of the change in the vortex shedding timing, the vortex dynamics are significantly different from those in the DS-I [Figs. 21(c)–21(g)]. When the cylinder is at the top (instant *i*), the gap-side shear layer separates into a vortex and pairs with the freestream-side vortex that formed a half-period earlier [Figs. 21(a) and 21(c)]. At this instant, the lift coefficient reaches its lowest value, while the drag coefficient is around the peak [Fig. 21(b)]. When the cylinder moves toward the bottom (from instant *ii* to *iii*), the freestream-side shear layer develops and saturates at instant *iii* [Figs. 21(a), 21(d), and 21(e)]. As for the forces, the drag coefficient decreases from the peak, whereas the lift coefficient increases monotonically. Furthermore, as the cylinder moves toward the wall, both the gap-side shear layer of the cylinder and the boundary layer develop, decreasing the passage of the gap flow from instant *ii* to *iii*. Correspondingly, the gap flow velocity decreases.

When the cylinder moves back from the bottom (from instant *iv* to *vi*), the freestream-side shear layer has just separated from the cylinder and shows direct interactions with the boundary layer. In contrast to that in the LB, the coalescence of the freestream-side vortex with the boundary layer is weaker [Fig. 21(g)]. In this half-period, the gap flow increases slightly, while an opposite behavior occurs for the drag and lift coefficients. As depicted in Fig. 21(b), the drag increases while the lift decreases monotonically.

IV. CONCLUSIONS

In this study, the VIV of a circular cylinder in proximity to a stationary wall was studied using 3D DNS at a subcritical Reynolds number of 500 and a gap ratio of 0.8. The cylinder could vibrate in both the transverse and streamwise directions. To explore the influences of the stationary wall and boundary layer, we studied the characteristics of the vibration response and vortex dynamics varying with the reduced velocity. Furthermore, we evaluated the wake three-dimensionality through instantaneous vortical structures, spanwise-averaged vorticity contours, and statistics of the enstrophies. Finally, the flow physics covering the response was analyzed through the time histories of the displacement, gap flow velocities, drag and lift coefficients, and vorticity contours in one vibration period. The main findings of this study are summarized as follows:

In the simulated U_r range, the vibration response can be divided into four regions: IB, LB, DS-I, and DS-II. The two DS regions appear at the two ends of the simulated U_r range, and because of the negligible amplitude, the vibration frequencies in these two regions closely follow the vortex shedding frequency (St) of the stationary case. In the IB, the amplitude increases sharply, and the vibration frequency lies between the natural frequency of the cylinder and the vortex shedding frequency of the stationary case, resulting in soft lock-in. In the LB, the amplitude increases further, and the vibration frequency approaches the natural frequency, leading to the presence of lock-in.

Because of the wall proximity, the dominant vibration frequencies in the two directions become identical, and the trajectories of the displacement differ contrastingly in each region. Figure-eight, combined figure-eight and raindrop, raindrop, and chaotic trajectories appear successively with increasing U_r, dominating DS-I, IB, LB, and DS-II, respectively. In addition, due to the presence of the stationary wall and boundary layer, the phase lag between the lift and displacement remains at 0° in DS-I, IB, and LB, while it jumps to 180° when transforming into the DS-II. This is significantly different from the VIV of an isolated circular cylinder, where the phase jump occurs in the middle of the LB.

In each region, the wake three-dimensionality and vortex dynamics vary considerably. The statistics of the enstrophies positively confirm that the wake three-dimensionality increases linearly with the amplitude. In the DS, the cylinder remains approximately stationary, and the vortex shedding of the cylinder is significantly influenced by the dynamics of the boundary layer and gap flow, resulting in dislocations along the span. In the IB and LB, the enlarged amplitude synchronizes the vortex shedding along the span and strengthens the vortex. As the cylinder moves closer to the stationary wall, the interactions of the vortices with the boundary layer become stronger. The gap-side shear layer becomes more irregular, while the vortices dissipate more quickly. The statistics of the gap flow indicate that its mean streamwise velocity is determined by the time-averaged gap, while the fluctuating streamwise velocity of the gap flow is governed by the amplitude. This suggests that through these two metrics we can predict the gap flow passage and structural vibration.

The flow physics of each region is also different. In the small-amplitude case, including the DS and IB, the boundary layer merges with the freestream-side vortex of the cylinder and forces the gap-side vortex to pair with the freestream-side vortex. The vortices go upward slightly when moving downstream. However, because of the suppression of the gap-side shear layer by the stationary wall and boundary layer, the gap-side vortices have gap strengths and dissipate more quickly in the wake. In the large-amplitude case, the gap-side shear layer collides with the boundary layer before separating from the cylinder and disintegrates into small parts directly. These small vortices dissipate very quickly, and as a result, only negative vortices exist in the wake.

ACKNOWLEDGMENTS

This work was financially supported by the National Natural Science Foundation of China (Grants No. 51779172, No. 51579175, and 51979186). The work was carried out at the National Supercomputer Center in Tianjin, and the calculations were performed in Tianhe 3 prototype.

---

[1] R. D. Blevins, *Flow-induced Vibrations* (Van Nostrand Reinhold, New York, 1990).

[2] T. Sarpkaya, A critical review of the intrinsic nature of vortex-induced vibrations, J. Fluids Struct. **19**, 389 (2004).

[3] C. H. K. Williamson and R. Govardhan, Vortex-induced vibration, Annu. Rev. Fluid Mech. **36**, 413 (2004).

[4] C. H. K. Williamson and R. Govardhan, A brief review of recent results in vortex-induced vibrations, J. Wind Eng. Ind. Aerodyn. **96**, 713 (2008).

[5] M. P. Païdoussis, S. J. Price, and E. De Langre, *Fluid-structure Interactions: Cross-flow Induced Instabilities* (Cambridge University Press, Cambridge, 2010).

[6] P. W. Bearman, Circular cylinder wakes and vortex-induced vibrations, J. Fluids Struct. **27**, 648 (2011).

[7] X. Wu, F. Ge, and Y. Hong, A review of recent studies on vortex-induced vibrations of long slender cylinders, J. Fluids Struct. **28**, 292 (2012).

[8] D. T. Tsahalis and W. T. Jones, Vortex-induced vibration of a flexible cylinder near a plane boundary in steady flow, in *Proceedings of the Thirteenth Annual Offshore Technology Conferences* (Houston, Texas, 1981), pp. 367–386.

[9] A. Kozakiewicz, B. M. Sumer, and J. Fredsøe, Spanwise correlation on a vibrating cylinder near a wall in oscillatory flows, J. Fluids Struct. **6**, 371 (1992).

[10] M. J. Chern, G. T. Lu, Y. H. Kuan, S. Chakraborty, G. Nugroho, C. B. Liao, and T. L. Horng, Numerical study of vortex-induced vibration of circular cylinder adjacent to plane boundary using direct-forcing immersed boundary method, J. Mech. **34**, 177 (2018).

[11] J. Fredsøe, B. M. Sumer, J. Andersen, and E. A. Hansen, Transverse vibration of a cylinder very close to a plane wall, J. Offshore Mech. Arct. Eng. **109**, 52 (1987).

[12] K. Raghavan, M. M. Bernitsas, and D. Maroulis, Effect of bottom boundary on VIV for energy harnessing at $8 \times 10^3 < \mathrm{Re} < 1.5 \times 10^5$, ASME J. Offshore Mech. Arct. Eng. **131**, 031102 (2009).

[13] B. Yang, F. P. Gao, D. S. Jeng, and Y. X. Wu, Experimental study of vortex-induced vibrations of a cylinder near a rigid plane boundary in steady flow, Acta Mech. Sin. **25**, 51 (2009).

[14] S. Fu, Y. Xu, and Y. Chen, Seabed effects on the hydrodynamics of a circular cylinder undergoing vortex-induced vibration at high Reynolds number, J. Waterway, Port, Coastal, Ocean Eng. **140**, 04014008 (2014).

[15] Z. Li, W. Yao, K. Yang, R. K. Jaiman, and B. C. Khoo, On the vortex-induced oscillations of a freely vibrating cylinder in the vicinity of a stationary plane wall, J. Fluids Struct. **65**, 495 (2016).

[16] W. Chen, C. Ji, D. Xu, and J. Williams, Two-degree-of-freedom vortex-induced vibrations of a circular cylinder in the vicinity of a stationary wall, J. Fluids Struct. **91**, 102728 (2019).

[17] W. Chen, C. Ji, D. Xu, and Z. Zhang, Vortex-induced vibrations of two inline circular cylinders in proximity to a stationary wall, J. Fluids Struct. **94**, 102958 (2020).

[18] D. M. Y. Tham, P. S. Gurugubelli, Z. Li, and R. K. Jaiman, Freely vibrating circular cylinder in the vicinity of a stationary wall, J. Fluids Struct. **59**, 103 (2015).

[19] J. M. D. Barbosa, Y. Qu, A. V. Metrikine, and E. M. Lourens, Vortex-induced vibrations of a freely vibrating cylinder near a plane boundary: Experimental investigation and theoretical modelling, J. Fluids Struct. **69**, 382 (2017).

[20] M. Zhao and L. Cheng, Numerical simulation of two-degree-of-freedom vortex-induced vibration of a circular cylinder close to a plane boundary, J. Fluids Struct. **27**, 1097 (2011).

[21] M. H. Chung, Transverse vortex-induced vibration of spring-supported circular cylinder translating near a plane wall, Eur. J. Mech. B Fluids **55**, 88 (2016).

[22] X. K. Wang, Z. Hao, and S. K. Tan, Vortex-induced vibrations of a neutrally buoyant circular cylinder near a plane wall, J. Fluids Struct. **39**, 188 (2013).

[23] Z. Li, R. K. Jainman, and B. C. Khoo, Coupled dynamics of vortex-induced vibrations and stationary wall at low Reynolds number, Phys. Fluids **29**, 093601 (2017).

[24] S. Daneshvar and C. Morton, On the vortex-induced vibration of a low mass ratio circular cylinder near a planar boundary, Ocean Eng. **201**, 107109 (2020).

[25] C. H. K. Williamson and A. Roshko, Vortex formation in the wake of an oscillating cylinder, J. Fluids Struct. **2**, 355 (1988).

[26] Y. Gao, L. Liu, L. Zou, Z. Zhang, and B. Yang, Effect of surface roughness on vortex-induced vibrations of a freely vibrating cylinder near a stationary plane wall, Ocean Eng. **198**, 106837 (2020).

[27] L. F. Chen and G. X. Wu, Flow-induced transverse vibration of a circular cylinder close to a plane wall at small gap ratios, Appl. Ocean Res. **103**, 102344 (2020).

[28] S. Peter and A. K. De, Characteristics of the wake behind a transversely oscillating cylinder near a wall, J. Fluids Eng. **139**, 031201 (2017).

[29] H. A. Van de Vorst, BI-CGSTAB: A fast and smoothly converging variant of BI-CG for the solution of nonsymmetric linear system, SIAM J. Sci. Stat. Comput. **13**, 631 (1992).

[30] C. S. Peskin, Flow patterns around heart valves: A digital computer method for solving the equations of motion, Ph.D. thesis, Yeshiva University, New York, 1972.

[31] C. Ji, A. Munjiza, and J. J. R. Williams, A novel iterative direct-forcing immersed boundary method and its finite volume applications, J. Comput. Phys. **231**, 1797 (2012).

[32] W. Chen, C. Ji, W. Xu, S. Liu, and J. Campbell, Response and wake patterns of two side-by-side elastically supported circular cylinders in uniform laminar cross-flow, J. Fluids Struct. **55**, 218 (2015).

[33] W. Chen, C. Ji, J. Williams, D. Xu, L. Yang, and Y. Cui, Vortex-induced vibrations of three tandem cylinders in laminar cross-flow: Vibration response and galloping mechanism, J. Fluids Struct. **78**, 215 (2018).

[34] W. Chen, C. Ji, and D. Xu, Vortex-induced vibrations of two side-by-side circular cylinders with two degrees of freedom in laminar cross-flow, Comput. Fluids **193**, 104288 (2019).

[35] X. K. Wang and S. K. Tan, Comparison of flow patterns in the near wake of a circular cylinder and a square cylinder placed near a plane wall, Ocean Eng. **35**, 458 (2008).

[36] E. Wang, Q. Xiao, and A. Incecik, Three-dimensional numerical simulation of two-degree-of-freedom VIV of a circular cylinder with varying natural frequency ratios at Re = 500, J. Fluids Struct. **73**, 162 (2017).

[37] W. Chen, C. Ji, M. M. Alam, and Y. Yan, Three-dimensional flow past two stationary side-by-side circular cylinders, Ocean Eng. **244**, 110379 (2022).

[38] N. Jauvtis and C. H. K. Williamson, The effect of two degrees of freedom on vortex-induced vibration at low mass and damping, J. Fluid Mech. **509**, 23 (2004).

[39] V. Yogeswaran Navrose, S. Sen, and S. Mittal, Free vibrations of an elliptic cylinder at low Reynolds numbers, J. Fluid Struct. **51**, 55 (2014).

[40] D. Kumar, A. K. Singh, and S. Sen, Identification of response branches for oscillators with curved and straight contours executing VIV, Ocean Eng. **164**, 616 (2018).

[41] C. W. Rowley, I. Mezic, S. Bagheri, P. Schlatter, and D. S. Henningson, Spectral analysis of nonlinear flows, J. Fluid Mech. **641**, 115 (2009).

[42] P. J. Schmid, Dynamic mode decomposition of numerical and experimental data, J. Fluid Mech. **656**, 5 (2010).

[43] M. R. Jovanovic, P. J. Schmid, and J. W. Nichols, Sparsity-promoting dynamic mode decomposition, Phys. Fluids **26**, 024103 (2014).

[44] J. Mizushima and Y. Ino, Stability of flows past a pair of circular cylinders in a side-by-side arrangement, J. Fluid Mech. **595**, 491 (2008).

[45] S. P. Singh and S. Mittal, Vortex-induced oscillations at low Reynolds numbers: Hysteresis and vortex shedding modes, J. Fluids Struct. **20**, 1085 (2005).

[46] T. K. Prasanth, S. Behara, S. P. Singh, R. Kumar, and S. Mittal, Effect of blockage on vortex-induced vibrations at low Reynolds numbers, J. Fluids Struct. **22**, 865 (2006).

[47] K. Menon and R. Mittal, On the initiation and sustenance of flow-induced vibration of cylinders: Insights from force partitioning, J. Fluid Mech. **907**, A37 (2021).

[48] J. I. Jiménez-González and F. J. Huera-Huarte, Vortex-induced vibrations of a circular cylinder with a pair of control rods of varying size, J. Sound Vib. **431**, 163 (2018).

[49] R. Bourguet and D. Lo Jacono, Flow-induced vibrations of a rotating cylinder, J. Fluid Mech. **740**, 342 (2014).

[50] T. K. Prasanth and S. Mittal, Vortex-induced vibrations of a circular cylinder at low Reynolds numbers, J. Fluid Mech. **594**, 463 (2008).

[51] G. V. Papaioannou, D. K. P. Yue, M. S. Triantafyllou, and G. E. Karniadakis, Three-dimensionality effects in flow around two tandem cylinders, J. Fluid Mech. **558**, 387 (2006).

[52] H. Jiang and L. Cheng, Hydrodynamic characteristics of flow past a square cylinder at moderate Reynolds numbers, Phys. Fluids **30**, 104107 (2018).

[53] F. Tong, L. Cheng, and M. Zhao, Numerical simulations of steady flow past two cylinders in staggered arrangements, J. Fluid Mech. **765**, 114 (2015).

[54] H. Jiang and L. Cheng, Strouhal-Reynolds number relationship for flow past a circular cylinder, J. Fluid Mech. **832**, 170 (2017).

[55] J. Thapa, M. Zhao, T. Zhou, and L. Cheng, Three-dimensional simulation of vortex shedding flow in the wake of a yawed circular cylinder near a plane boundary at a Reynolds number of 500, Ocean Eng. **87**, 25 (2014).

[56] H. Jiang, Wake transition of a circular cylinder, Ph.D. thesis, The University of Western Australia, 2017.

[57] A. Munir, M. Zhao, H. Wu, L. Lu, and D. Ning, Three-dimensional numerical investigation of vortex-induced vibration of a rotating circular cylinder in uniform flow, Phys. Fluids **30**, 053602 (2018).

[58] C. H. K. Williamson, Three-dimensional wake transition, J. Fluid Mech. **328**, 345 (1996).

[59] H. Mansy, P.-M. Yang, and D. R. Williams, Quantitative measurements of three-dimensional structures in the wake of a circular cylinder, J. Fluid Mech. **270**, 277 (1994).